Electrochemical Reduction of CO_2 Using MoS_2-based Catalysts

Yashan Peng

In partial fulfilment of the requirements for the degree of

Master of Science

In Materials Science and Engineering

At the Delft University of Technology

To be defended publicly on 27th November of 2020 at 14:00

TU Delft Delft University of Technology

Student number	4903978

Daily Supervisors

Dr. Peyman Taheri	Delft University of Technology
Dr. Majid Ahmadi	University of Groningen

Thesis committee

Dr. Peyman Taheri	Delft University of Technology
Dr. Majid Ahmadi	University of Groningen
Dr. Urša Tiringer	Delft University of Technology
Dr. Yaiza Gonzalez Garcia	Delft University of Technology
Dr. Luana Mazzarella	Delft University of Technology
Eszter Mádai (PhD candidate)	Delft University of Technology

Abstract

Heavy dependence on fossil fuels has caused an astonishing growth in atmospheric CO_2 levels for the past decades. The increase of anthropogenic CO_2 emissions accelerates global warming and sea-level rising, which could lead to irreversible environmental damages. Electrochemically converting CO_2 to value-added fuels is a promising approach to reduce carbon footprint and store over-generating renewable electricity as chemical energy. Studies have shown the excellent catalytic performance of bulk MoS_2 concerning the low overpotential and high product selectivity towards CO for electrochemical CO_2 reduction reaction (CO_2RR) in ionic liquid-based solutions. However, its performance in different configurations and electrolytes remains unexplored. In this study, two types of MoS_2, namely bulk MoS_2 and MoS_2 film coated on a glassy carbon electrode (GCE), were used. Their CO_2RR performance in the $KHCO_3$ aqueous and ionic liquid-based solutions was investigated using electrochemical methods, gas chromatography (GC), and attenuated total reflectance - Fourier transform infrared spectroscopy (ATR-FTIR). Additionally, the photochemical activity of MoS_2 was explored using scanning vibrating electrode technique (SVET).

The selected catalysts were characterized before and after the CO_2 reduction process using scanning electron microscopy (SEM), energy-dispersive X-ray spectroscopy (EDS), and X-ray photoelectron spectroscopy (XPS). GC measurement results showed that MoS_2 film coated on GCE exclusively catalyzed H_2 evolution in aqueous solutions. It was also observed that higher activity was achieved on the MoS_2 film mixed with glassy carbon powder. Furthermore, the MoS_2 film with the changed bandgap structure also performed better in ionic liquid-based aqueous electrolyte. These findings suggest that the catalytic performance of MoS_2 film for CO_2RR could be enhanced by interspersing materials with high conductivity or modifying the bandgap structure.

Acknowledgements

During this research project, I have received much help. I would like to take this opportunity to thank those people who have helped me.

Firstly, I would like to express my sincere gratitude to my supervisors Dr. Peyman Taheri and Dr. Majid Ahmadi for their valuable guidance and extensive support throughout this project. My special thanks go to Dr. Marilia Moura de Salles Pupo and Shilong Fu for helping me with GC measurements. The constructive suggestions provided by Dr. Urša Tiringer are also greatly appreciated. I would also like to thank Dr. Yaiza Gonzalez Garcia for inspiring my interest in electrochemistry.

I am profoundly grateful to Agnieszka Kooijman for teaching me how to use the instruments in the labs. Besides, I would like to extend my thanks to the technicians and student assistants, including Sander van Asperen, Remko Seijffers, Kees Kwakernaak, Ton Riemslag, María Terol Sanchez, Katja Jarc, and Luis de Almeida Nieto.

I would like to express my great appreciation to Eszter Mádai and Khatereh Roohi for spending their time reading my thesis and giving me feedback. Finally, I would like to thank my family and friends for their support and encouragement.

Yashan Peng
Delft, Nov 2020

Contents

List of Figures

List of Tables

Acronyms

ATR-FTIR Attenuated Total Reflectance Fourier-transform Infrared Spectroscopy

CA Chronoamperometry

CO_2RR Electrochemical CO_2 Reduction Reaction

CV Cyclic Voltammetry

DFT Density Functional Theory

EDS Energy-Dispersive X-ray Spectroscopy

FE Faradaic Efficiency

FID Flame Ionisation Detector

GC Gas Chromatography

GCEs Glass Carbon Electrodes

GCP Glass Carbon Powder

HER Hydrogen Evolution Reaction

HPLC High Performance Liquid Chromatography

IHP Inner Helmholtz Plane

ILs Ionic Liquids

NMR Proton Nuclear Magnetic Resonance

OER Oxygen Evolution Reaction

OHP Outer Helmholtz Plane

TMDCs Transition-metal Dichalcogenides

RHE Reversible Hydrogen Electrode

SCE Saturated Calomel Electrode

SEM Scanning Electron Microscopy

SVET Scanning Vibrating Electrode Technique

TCD Thermal Conductivity Detector

XPS X-ray Photoelectron Spectroscopy

1

Introduction

1.1. CO_2 Emission

The atmospheric CO_2 concentration has steadily risen in the past decades (Fig. 1.1a), which accelerates global warming and climate change. It is estimated that the global average temperature will be 1.5 °C warmer than pre-industrial levels during 2030 - 2052. In addition, without any significant progress in the process of CO_2 emission reduction by 2100, the average sea level would rise by 1 m [1–3]. Although the ocean could absorb approximately 30% CO_2 in the air, this leads to ocean acidification. The acidity of the ocean's surface waters has increased by 30% since the Industrial Revolution [4]. These climate changes pose a threat to the balance of our environment.

According to the Intergovernmental Panel on Climate Change (IPCC), limiting global warming to 1.5 °C will require drastic transitions in many sectors, and global human-caused CO_2 emissions need to reach net-zero by 2050 [3]. The primary source of CO_2 emission caused by human activities is fossil fuels, and they are expected to continue to dominate for the next decades [7, 8]. The intermittent nature of renewable energy sources is still limiting their widespread usage because storing the power from these sources remains challenging [9]. Converting CO_2 into fuels and other value-added products is a promising strategy to address the energy storage issues and close the carbon cycle. Figure 1.1b illustrates how CO_2 reduction helps to achieve a carbon-neutral energy cycle. Numerous studies have been conducted to improve CO_2 conversion techniques; however, many challenges prevent them from commercialization, such as low energy efficiency and overall conversion rate [10, 11].

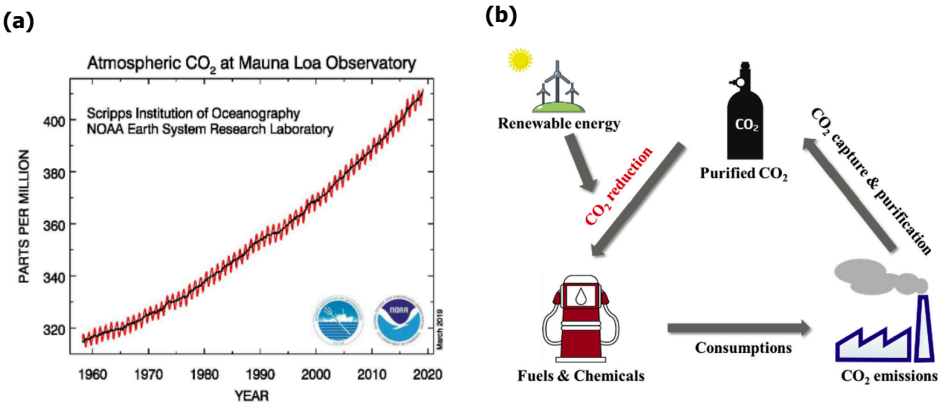

Figure 1.1: (a) The CO_2 levels in the air during 1960-2020. Adapted from [5]. (b) The role of electrochemical CO_2 reduction in the carbon cycle. Adapted from [6].

1.2. CO_2 Conversion Technologies

The main approaches for CO_2 conversion can be classified into (1) chemical catalytic process including electrochemical, thermochemical, and photochemical reactions, (2) biological process, and (3) physical process [12, 13]. Electrochemical CO_2 reduction reaction (usually denoted as CO_2RR in literature) is more appealing among these methods because of (1) the useful products, such as CO and CH_4, generated through the process, (2) the ability to couple with clean energy sources like solar and wind power, (3) the controllability of process by adjusting applied potentials, temperatures, and electrolytes, (4) the technical and economic feasibility [12, 13]. However, the CO_2 molecule is very stable; therefore, activation of the CO_2 reduction reaction requires a substantial amount of electricity. Electrocatalysts are applied to lower the energy barriers since they can form a chemical bond between CO_2 and catalyst, stabilizing reaction intermediates [11]. An appropriate selection of catalysts dramatically influences the energy efficiency and cost of electrochemical CO_2 reduction systems.

1.3. Research Objectives

In recent years, molybdenum disulfide (MoS_2), a member of transition-metal dichalcogenides (TMDCs), has gained significant attention in the field of electrochemical CO_2 reduction thanks to its promising electrocatalytic performance in ionic liquid [14]. However, investigation of electrocatalytic CO_2 reduction on MoS_2 surface is still at early stages with some crucial information remaining unclear, such as reaction paths and mechanisms, active catalyst sites, and structural impacts. Furthermore, there are few reports regarding the electrocatalytic performance of MoS_2 towards

the reduction of CO_2 in aqueous media. Therefore, the main objective of this work is to investigate the activity, selectivity, and stability of MoS_2 as the catalyst for CO_2RR.

1.4. Approach

The glass carbon electrodes (GCEs) were coated with MoS_2 nanopowder by the drop-casting method. The modified GCEs were compared with the bulk MoS_2. Electrochemical activity and stability of MoS_2 were examined using conventional electrochemical techniques in the three-electrode system. The photoelectrochemical performance was explored by scanning vibrating electrode technique (SVET). Product analysis was performed by gas chromatography (GC) and Fourier-transform infrared spectroscopy (ATR-FTIR). MoS_2 chemical composition and morphology were analyzed by scanning electron microscopy (SEM), energy-dispersive X-ray spectroscopy (EDS), and X-ray photoelectron spectroscopy (XPS).

1.5. Report Outline

A brief description of the context of this study and the research objectives is given in Chapter 1. Chapter 2 deals with the theoretical background and the current state of research in the field of electrocatalytic CO_2 reduction. This is followed by a description of the experimental setup, operation parameters, product analysis methods, and characterization techniques used over the course of this work in chapter 3. The results of CO_2RR experiment and surface characterization are discussed in chapter 4. The conclusion of this research and recommendations for future work are displayed in chapter 5 and 6, respectively. The supporting information for this study is added in appendices.

2

Theory

The important theories behind CO_2RR for understanding the contents of this thesis are provided in this chapter. It starts with the fundamentals of CO_2RR, followed by the discussion on the potentials of CO_2 reduction on MoS_2 surface, and ends with the description of the parameters used to compare catalytic performances in literature.

2.1. Thermodynamic Perspectives of CO_2 Electroreduction

Conversion of CO_2 can happen through different routes with different products. CO_2 reduction driven by renewable electricity on the surface of an appropriate electrocatalyst offers a promising approach to convert CO_2 into fuels and commodity chemicals. The first step of CO_2 reduction is associated with one-electron transfer to form the $CO_2^{\bullet-}$ radical intermediate. However, this step has a highly negative redox potential (-1.9 V versus standard hydrogen electrode in water) [11]. Nonetheless, with the assistance of catalysts, CO_2 reduction can occur at less negative redox potential without the formation of CO_2 anion radicals. This reaction path is related to proton-assisted multiple-electron transfer. CO_2 can be converted into many products based on the number of protons and electrons transferred [13]. Table 2.1 lists the common products transformed from CO_2 and the corresponding reduction reactions and equilibrium potentials. The common final products include formic acid ($HCOOH$), carbon monoxide (CO), ethylene (C_2H_4), methanol (CH_3OH), ethanol (C_2H_5OH) and methane (CH_4). In reality, CO_2RR requires more negative potentials than thermodynamics predicts due to the sluggish kinetics of CO_2RR. Besides, a less negative equilibrium potential of a reduction reaction does not mean that the reaction is more likely to occur. CO_2RR is also kinetically dependent on the avail-

ability of protons in an electrolyte, implying that the hydrogenation of adsorbed C1 intermediates is more kinetically favorable than C2 and higher hydrocarbon formation [13].

Although CO_2RR is viable from a thermodynamics perspective, there are still some challenges regarding the electrocatalytic reduction of CO_2: (1) the linear CO_2 molecule is stable and chemically inert with a low electron affinity [15]. Additionally, (2) CO_2 transformation is dominated by nucleophilic attacks at the carbon, which is an uphill process requiring a substantial input of energy (~750 kJ mol^{-1} needed for dissociation of C=O bond, while breaking the O-H bond in H_2O consumed only 463 kJ mol^{-1}) and, (3) CO_2RR usually takes place in an aqueous electrolyte with competitive cathodic Hydrogen evolution reaction (HER) [12, 13].

Table 2.1: Equilibrium Potentials for CO_2RR. OER and HER are also included. Adapted from [16].

Reaction	E^0/[V vs. RHE]	Product
$2\,H_2O \longrightarrow O_2 + 4\,H^+ + 4\,e^-$	1.23	OER
$2\,H^+ + 2\,e^- \longrightarrow H_2$	0	HER
$xCO_2 + nH^+ + ne^- \longrightarrow \text{product} + yH_2O$		CO_2RR
$CO_2 + 2\,H^+ + 2\,e^- \longrightarrow HCOOH_{(aq)}$	-0.12	Formic acid
$CO_2 + 2\,H^+ + 2\,e^- \longrightarrow CO_{(g)} + H_2O$	-0.10	Carbon monoxide
$CO_2 + 8\,H^+ + 8\,e^- \longrightarrow CH_{4(g)} + 2\,H_2O$	0.17	Methane
$2\,CO_2 + 12\,H^+ + 12\,e^- \longrightarrow C_2H_5OH_{(aq)} + 3\,H_2O$	0.09	Ethanol
$2\,CO_2 + 12\,H^+ + 12\,e^- \longrightarrow C_2H_{4(g)} + 4\,H_2O$	0.08	Ethylene

2.2. Electrochemical Cell Types

A cathodic reaction for CO_2RR can be represented by Eq. 2.1. Products converted from CO_2 are associated with the applied potential and the selection of catalysts. Not all cathodic reactions are desired. The competition of HER, as indicated in Eq. 2.2, leads to overall efficiency loss.

$$xCO_2 + nH^+ + ne^- \longrightarrow \text{product} + yH_2O \tag{2.1}$$

$$2\,H^+ + 2\,e^- \longrightarrow H_2 \tag{2.2}$$

$$2\,H_2O \longrightarrow O_2 + 4\,H^+ + 4\,e^- \tag{2.3}$$

The counter reaction for CO_2RR is the oxygen evolution reaction (OER) taking place at the anode via Eq. 2.3. The anodic half-reaction is also crucial for improving

the energy efficiency of CO_2RR cells because the protons generated in OER can join as a reactant for the later CO_2 reduction. Moreover, the overall cell potential involves both anodic and cathodic processes, thereby reducing the OER overpotential can also help increase the energy efficiency of CO_2RR systems [13].

H-type cells are commonly used in the CO_2 electroreduction setup. It is a three-electrode system as shown in Fig. 2.1a. The working and reference electrodes are placed in one chamber for cathodic reactions, while the counter electrode is in the other chamber for anodic reactions. The two compartments are separated by a proton-exchange membrane, which prevents the migration of the reduced products from cathode to anode.

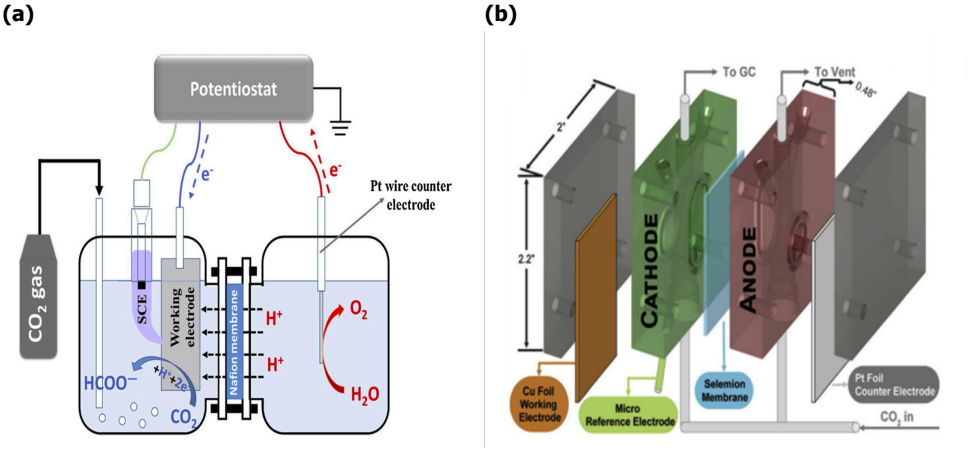

Figure 2.1: Schematic illustration of electrochemical cell types. (a) A conventional H-type cell. (b) A flow cell. Adapted from [17].

As illustrated in Fig. 2.1b, a sandwich-like cell (flow-cell) design was proposed to increase the concentration of liquid products for better detection. In comparison to the typical H-cell, the working electrode and counter electrode in this setup were put parallel to each other with a small distance and separated by the membrane. The small reference electrode was placed close to the working electrode by inserting it into the cathodic chamber, diminishing the solution resistance between these two electrodes. This modified H-cell setup enlarged the working electrode surface and shrank the electrolyte volume so that an elevated proportion of the electrode surface area to the electrolyte volume (S/V) was obtained, commonly larger than 0.5 [17]. As a result, the concentration of liquid products could quickly reach the quantitative detection range of the analytical equipment, e.g., nuclear magnetic resonance (NMR) or high pressure liquid chromatography (HPLC). In addition, the continuous CO_2 gas flowing through the cathodic chamber can carry gaseous products pro-

duced at the cathode to gas chromatography (GC) where the gaseous products are identified. The CO_2 flow rate should be sufficiently high to mix uniformly with gaseous products and maintain the saturation of CO_2 in the solution; nonetheless, the flow rate must be well controlled to avoid diluting the concentration of gaseous products below the detection limits of GC. A disadvantage of the cell design with a high S/V ratio is that the dissolved CO_2 concentration becomes under-saturated quickly, causing an increase of Faradaic efficiency for H_2 [18].

2.3. Reaction Media

The electrolytes in CO_2RR are used to support ion transport and electrode reactions. The selection and concentration of the supporting electrolytes are a crucial factor to improve catalytic performance. However, impurities from the electrolyte could also poison the active sites of catalysts leading to catalytic deactivation. When the electrode is negatively charged, positive ions in the electrolyte are attracted to the electrode surface, forming a region where charged species and oriented dipoles accumulate [6]. The region is called the electrical double layer (Fig. 2.2). The interface structure can be divided into five different regions, which are the electrode surface, the inner Helmholtz plane (IHP), the outer Helmholtz plane (OHP), the diffuse layer, and the bulk solution [6, 19]. The inner layer accommodates specifically adsorbed reactants, reaction intermediates, reaction products, solvent molecules, and solvated electrolyte ions, while the outer layer contains solvated ions that are of opposite charge to the electrode. The compact layer is comprised of the IHP and the OHP layers. The zone between the OHP and the bulk solution is the diffuse layer consisting of non-specifically adsorbed ions. Beyond the diffuse layer is denoted as the bulk, where the potential of the electrode can not influence the electrolyte structure anymore. The compact layer, combined with the diffuse layer, is called the electrical double layer. The total charge density of the electrode is equal to that of the electrical double layer, but their charge signs are opposite [19]. The double-layer structure is subjected to the change of potential-dependent structure of the solvent, reaction-induced concentration gradients, and potential-dependent behavior of electrolyte cations, which also affects CO_2RR activity and product selectivity [20].

2.3.1. Aqueous Solutions

The common aqueous electrolytes applied in CO_2RR are weakly acidic or alkaline solutions containing inorganic salts, which consist of alkali metal cations, such as Na^+ and K^+, and HCO_3^-, Cl^- or SO_4^{2-} anions [13]. Cation species can change the OHP potential influencing the distribution of charged species near the electrode and the hydrogen coverage on the electrode. Cation size is also demonstrated to affect product selectivity [21]. Larger cations could inhibit HER [22]. HER dominates over CO_2RR in Li^+ solutions, whereas the situation is reversed in Na^+, K^+, and Cs^+

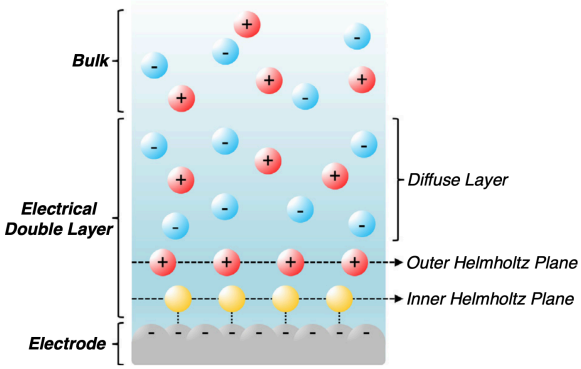

Figure 2.2: Schematic diagram of the double layer structure at the cathode. Adapted from [20].

electrolytes.

Anion species could also affect product selectivity by altering the local pH at the electrode [23]. A high local pH suppresses HER due to the low proton level. Forming CH_4 is favored in concentrated $KHCO_3$ solution, whereas C_2H_4 and alcohols are preferentially generated in dilute $KHCO_3$ electrolyte under a non-equilibrium local high pH. In other words, the product ratio of CH_4 to C_2H_4 raises at higher HCO_3^- level.

The low solubility of CO_2 (0.033 M) in aqueous electrolytes at ambient conditions sets a limit on the maximum current density for CO_2RR. Furthermore, the number of electrochemically active CO_2 molecules in the electrolyte is subject to the change of the solution pH value. As Eq. 2.4 shows, with increasing pH values, the carbonic acid equilibrium shifts to form bicarbonate and carbonate, causing a decrease in the amount of active CO_2 [24].

$$CO_{2(aq)} + H_2O \rightleftharpoons H_2CO_3 \rightleftharpoons H^+ + HCO_3^{2-} \rightleftharpoons 2\,H^+ + CO_3^{2-} \qquad (2.4)$$

In addition to the impact of CO_2 solubility, the solution pH value influences the thermodynamics of CO_2RR. Figure 2.3 demonstrates how the electrochemical equilibrium phases of carbon in an aqueous solution can be affected by the potential and pH. CO_2RR at low pH values requires less negative potential according to thermodynamics, which is more energetically preferred; however, the competing H_2 evolution is also thermodynamically favorable in acid media.

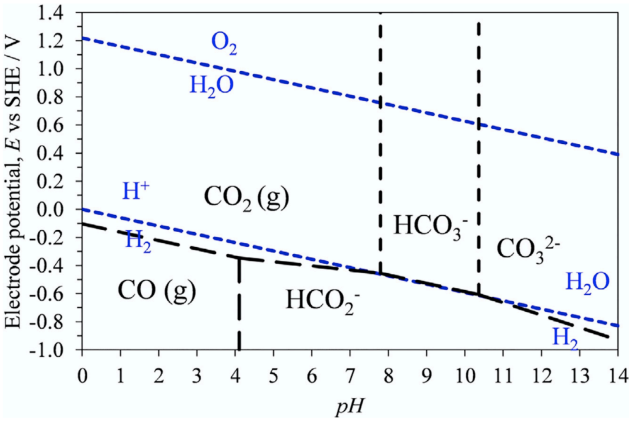

Figure 2.3: Pourbaix Diagram for a C-H_2O System at 298 K and 1 Bar. Adapted from [24].

2.3.2. Ionic Liquids

Ionic liquids, which are salts in the liquid state, have received extensive attention for their unique properties, e.g., outstanding gas solubility, ionic conductivity and, thermal stability [25]. Solutions mixed with ionic liquids (ILs) and aqueous electrolytes have been demonstrated as good media for CO_2RR [26]. The common ILs applied in CO_2RR contain [EMIM]-[BF_4], [EMIM]-[TFO], [BMIM]-[OTF]. In general, using ILs could reduce CO_2RR overpotential, suppress HER, raise the CO_2 solubility, enhance CO_2RR current densities, adjust solution pH, stabilize reactive intermediates, and increase the product selectivity toward CO formation. $[EMIM]^+$ cations can react with dissolved CO_2, forming $[EMIM\text{-}CO_2]^+$ complexes. The adsorption of these complexes on the cathode increases the local CO_2 concentration near the electrocatalyst surface, promoting CO_2RR. Additionally, $[EMIM\text{-}CO_2]^+$ complexes could act as an inhibitor for H_2 evolution by blocking the electrocatalytic surface, thereby the available protons in the solution are utilized exclusively for CO_2RR [27, 28]. Furthermore, the presence of hydroxyl ions (e.g., $[BF_3OH]^-$,$[BF_2(OH)_2]^-$, and $[BF(OH)_3]^-$) formed by [EMIM]-[BF_4] hydrolysis could lower solution pH and increase proton availability, which improves the rate of CO_2RR [13].

Due to the high viscosity and cost, ILs are often mixed with water for electrolyte use. The reported ILs concentrations in the literature exhibit a wide range. The more ILs added does not guarantee the higher current density. Research by Asadi *et al.* shows that a solution with 96% water and 4% EMIM-BF_4 performed better in terms of current density than the aqueous solutions with 10% and 0% [EMIM]-[$BF]_4$ on bulk MoS_2 (Fig. 2.5b). Optimized ILs ratios for the vital catalyst materials still need to be discovered. In despite of the benefits ILs offer, their potentials are still limited by the high cost and poor stability in water-based media. [13].

2.4. Catalytic Performance Indicators

The common performance indicators employed to compare CO_2RR systems are introduced in this section.

Faradaic Efficiency (FE%)

Selectivity for the desired product is a critical factor in evaluating catalytic performance, owing to multiple reactions taking place simultaneously at the cathode during CO_2RR. High selectivity can prevent wasting electricity on undesired products and also be beneficial to the product separation process. Product selectivity is normally expressed in terms of product Faradaic efficiency (FE%) calculated by Eq. 2.5 where n_x is the number of moles of product x obtained by electrolysis at a certain potential, Z_x is the number of electrons transferred per mole of the product x, F is the Faraday constant, and Q is the total charge consumed by the electrolysis [6].

$$FE_x\% = \frac{n_x Z_x F}{Q} \times 100 \tag{2.5}$$

Overpotential (η)

To obtain a considerable amount of the desired product requires a much more negative potential than the one thermodynamic predicted. The absolute value of the difference between these two potentials is called overpotential (η) expressed in Eq. 2.6 [6].

$$\eta = |E - E^{eq}| \tag{2.6}$$

Current density

The reaction rate in CO_2RR systems can be reflected by the current density which is defined as the ratio of the measured current to the geometric surface area of the working electrode. A partial current density of a specific product (equivalent to $FE_x\% \times$ overall current density) is often considered for comparison due to the multiple possible products.

Reversible Hydrogen Electrode

The applied potentials in literature are often reported versus the reversible hydrogen electrode (RHE). The reference electrode used in this study is either an Ag/AgCl or a saturated calomel electrode (SCE); however, the potentials with respect to them are pH-dependent. In order to compare with literature and offset the pH dependency, the applied potentials in this work are all converted to RHE via the following equations [29–31].

$$E_{SHE} = E_{Ag/AgCl} + E^0_{Ag/AgCl} \tag{2.7}$$

$$E_{SHE} = E_{SCE} + E^0_{SCE} \tag{2.8}$$

Where $E^0_{Ag/AgCl}$ = 0.1976 V at 25°C, E^0_{SCE} = 0.244 V at 25°C, $E_{Ag/AgCl}$ and E_{SCE} are the applied potentials.

$$E_{RHE} = E_{SHE} + 0.0591 \times pH \tag{2.9}$$

2.5. Potential Catalytic Materials for CO_2 Electroreduction

2.5.1. Metal Catalysts

Metal electrodes used for CO_2RR can be classified into four groups based on the type of reaction products (Fig. 2.4) [10]. The first group contains metallic copper solely. It is the only heterogeneous catalyst that shows remarkable selectivity and activity for CO_2RR product selectivity towards hydrocarbons [16]. The second group including Au, Ag and Zn produces CO as the primary product. The third group consisting of In, Pb, Sn and Cd, yielding formate as the major product, while the fourth group containing Ni, Fe, Pt and Ti obtains only H_2. It is worth of noting that CO is adsorbed strongly on metals of the fourth group, preventing further reduction of CO_2, thereby resulting in HER.

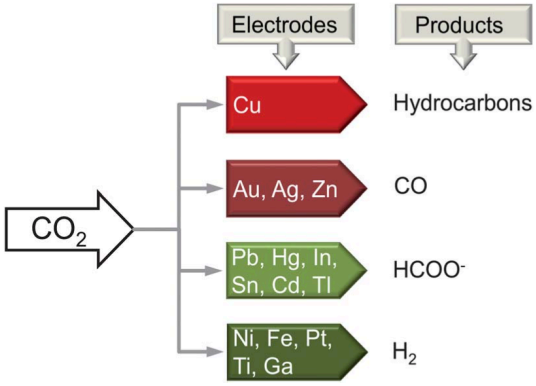

Figure 2.4: Common metal materials for CO_2RR electrodes and their main reaction products. Adapted from [10].

2.5.2. Transition-metal Dichalcogenides (TMDCs) catalysts

Searching for cost-effective CO_2RR electrocatalysts with high product selectivity remains a challenge for large-scale production. Noble metals such as Au and Ag have been considered the best choice for electrocatalysts in the conversion of CO_2 to CO [32]. Recently, MoS_2, a typical member of transition metal dichalcogenides (TMDCs), has gained significant attention for its remarkable electrocatalytic performance for CO production in ILs-based solutions. The study by Asadi *et al.* has displayed 98 FE% for CO at -0.764 V vs. RHE (Fig. 2.5a) in 96 mol% water - 4 mol% [EMIM]-[BF_4] electrolyte. This finding makes MoS_2 a potential candidate for replacing expensive noble metals in CO generation. MoS_2 has been widely utilized to catalyze the hydrogen evolution reaction (HER) in the water-splitting process; nevertheless, the researches for CO_2RR over MoS_2 are still in preliminary stage [33]. There are three main features of CO_2RR on MoS_2: (1) the low overpotential (about 54 mV) in ILs; (2) the high selectivity towards CO; (3) the tunable bandgap structure of MoS_2 allowing its photochemical catalysis [34]. The CO_2 reduction efficiency of MoS_2 can also be considerably improved by doping metallic atoms to modulate the electronic properties of the edge structure, thus altering the binding energies of reaction intermediates [14, 35].

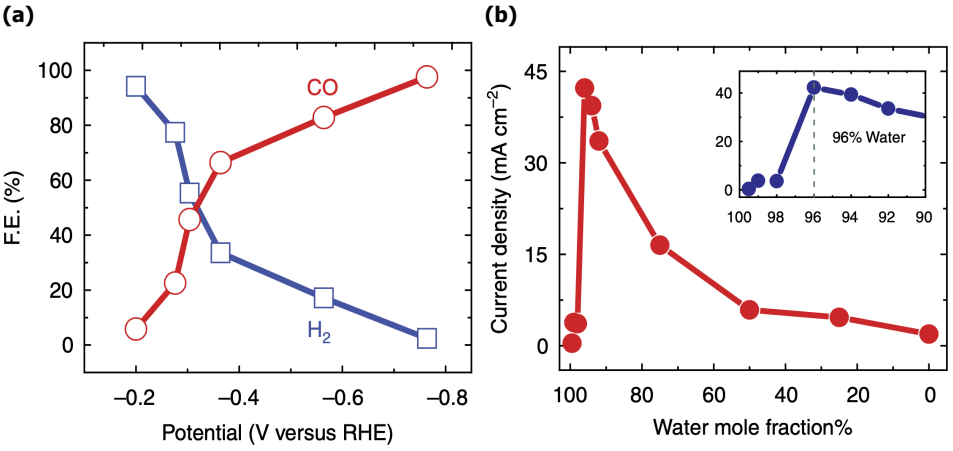

Figure 2.5: CO_2 reduction performance of the bulk MoS_2 catalyst in the [EMIM]-[BF_4] solution. (a) CO and H_2 Faradaic efficiency (FE) at different applied potentials. (b) The current density of CO_2 reduction (measured by Chrono-Amperometry) at 0.764 V versus RHE as a function of water mole fraction in [EMIM]-[BF_4] electrolyte. The maximum current density was recorded in 96 mol% water - 4 mol% [EMIM]-[BF_4] electrolyte (inset). Adapted from [27].

2.5.3. MoS_2 Structure and Properties

A monolayer of MoS_2 has an S-Mo-S sandwich structure, where the molybdenum plane is in between of 2 sulfide planes. Bulk MoS_2 is composed of stacked mono-

layers connected by weak van der Waals forces, resulting in the ease of being mechanically exfoliated to 2-D sheets. In general, a single layer has a thickness of approximately 0.65 nm [36]. MoS_2 can have two types of phases: trigonal prismatic phases and octahedral phases as represented in Fig. 2.6. The trigonal prismatic phase, which is conventionally referred to as the 2H phase (the digit indicates the number of layers in the unit cell), has a hexagonal symmetry corresponding to the trigonal prismatic coordination of the metallic atoms [37]. The octahedral phase, often referred to as the 1T phase, possesses a tetragonal symmetry corresponding to the octahedral coordination of the metallic atoms. Of these, the 1T and 3R polytypes are meta-stable [38]. The 1T structure exhibits metallic behavior, while both 2H and 3R structures show semiconducting behavior [39]. The transition from the semiconducting phase (2H) to the metallic phase (1T) has been reported by previous studies [38–40].

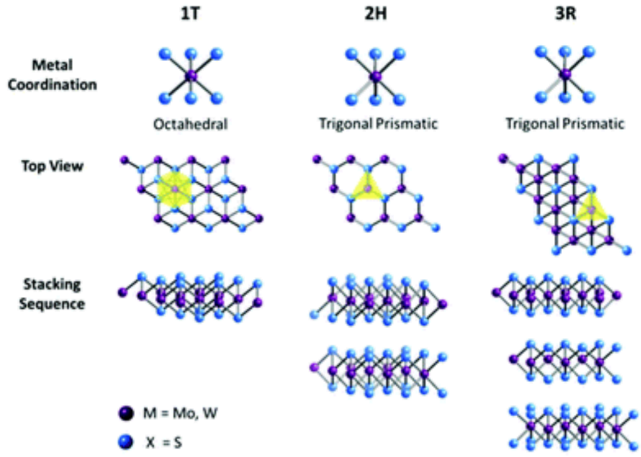

Figure 2.6: Different polytypes of MoS_2. Metal coordination can be octahedral or trigonal prismatic. The octahedral coordination allows stacking sequences yielding a tetragonal symmetry (1T). Different stacking sequences of trigonal prismatic monolayers can lead to various symmetries: hexagonal symmetry (2H) and rhombohedral symmetry (3R). Adapted from [39].

The electronic and optical properties of MoS_2 could be modified by altering the bandgap, which results from the confinement effect [41]. Bulk MoS_2 is a semiconductor with an indirect bandgap of 1.3 eV. In contrast, monolayer MoS_2 has a direct bandgap of 1.9 eV, which falls in the visible-light region and is sufficient for inducing photocatalytic reactions [38]. The bandgap is also tunable through introducing strain into the structure [42]. Moreover, nanoscale MoS_2 has excellent charge carrier mobility and a high ratio of surface-to-volume [43]. These advantages make a single-layer MoS_2 also a promising catalyst for photoelectrochemical applications.

2.5.4. Reaction Mechanism on MoS_2 Surface

The density functional theory (DFT) calculations in literature have shown strong binding interactions between Mo-exposed edge sites of MoS_2 and the adsorbed intermediates [34, 44]. This finding is further supported by the calculated density of states of the edge Mo atoms that indicate d-band centers of Mo-exposed edges are much closer to the Fermi level than metal catalysts. Figure 2.7 shows the hypothesized reaction pathways for CO_2 reduction at MoS_2 edges according to the existing DFT calculations.

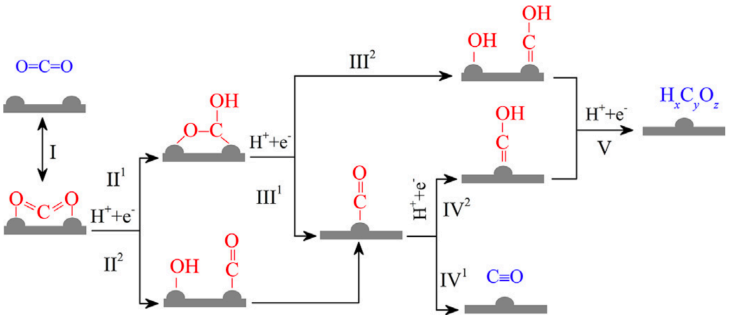

Figure 2.7: Projected reaction pathways for CO_2RR at the edge of MoS_2. The blue molecules are isolated products and the red ones are reaction intermediates. The grey bases and the semi-cylindrical hills represent the MoS_2 edges and active sites, respectively. The reactions of OH^* and H_2O^* are omitted. Adapted from [33].

Reaction step I is the adsorption and activation of the CO_2 molecule at two neighboring Mo atom sites where the C-O bonds are reconstructed, while step II refers to the hydrogenation process of CO_2 [33]. There are two different development direction for step II: reaction II^1 is $CO_2^* + H^+ + e^- \rightarrow COOH^*$. Reaction II^2 is $CO_2^* + H^+ + e^- \rightarrow HO{-}CO^* \rightarrow OH^* + CO^*$. The proposed reaction step III is the hydrogenation of $COOH^*$, which has two possible reactions (i.e., reaction III^1 and III^2). Reaction III^1 produces the same product of CO* as reaction II^2, and reaction step III^2 results in hydrocarbon species HxCyOz. There are two different paths to convert CO_2 to CO : (1) $I \rightarrow II^1 \rightarrow III^1 \rightarrow IV^1$; (2) $I \rightarrow II^2 \rightarrow IV^1$. However, the second pathway is more favorable because the activation barrier of reaction II^2 (1.01 eV) is lower than that of II^1 (1.92 eV). Furthermore, the formation of hydrocarbon products ($H_xC_yO_z$) is unlikely to take place due to the high adsorption energy of H on MoS_2, leading to the high product selectivity for CO [33, 45].

3

Experimental Method

This chapter describes the method for preparing the working electrode, the experimental setup, and characterization techniques used in this study. The ink formulas for drop-casting MoS_2 on glassy carbon support are discussed, followed by a brief overview of the various approaches for electrochemical measurements. The techniques used to analyze products of CO_2RR and characterize pre- and post-reaction catalysts are also presented.

3.1. Fabrication of the Electrodes

Working electrodes were prepared by drop-casting MoS_2 ink on glassy carbon plates (25mm×25mm×1mm, Hochtemperatur-Werkstoffe GmbH) and Germanium crystals. The former was for electrochemical measurement use, and the latter was for ATR-FTIR analysis use. Glassy carbon is electrochemically inert in a broad potential range, making it an ideal substrate for electrochemical research. Drop-casting, which means placing drops of nanoparticle dispersion on the substrate surface and allowing it to dry under controlled conditions, is a quick and easy method to deposit films (Fig. 3.1a) [46]. On the other hand, one disadvantage of this technique is the difficulty in controlling film thickness. The variables influencing the film thickness include the dropping volume and concentration. The film structure depends on the drying process, substrate wetting, and the evaporation rate [47].

The inks for drop-casting on glassy carbon consisted of MoS_2 nanopowder (90 nm diameter, Sigma-Aldrich), Nafion (serving as a binder, Sigma-Aldrich), DI water, and isopropanol. Water is not a good solvent for drop-casting due to the low vapor pressure and large surface tension, thus alcohol can be used to replace water [46]. However, nanoparticle dispersions with a high concentration of isopropanol

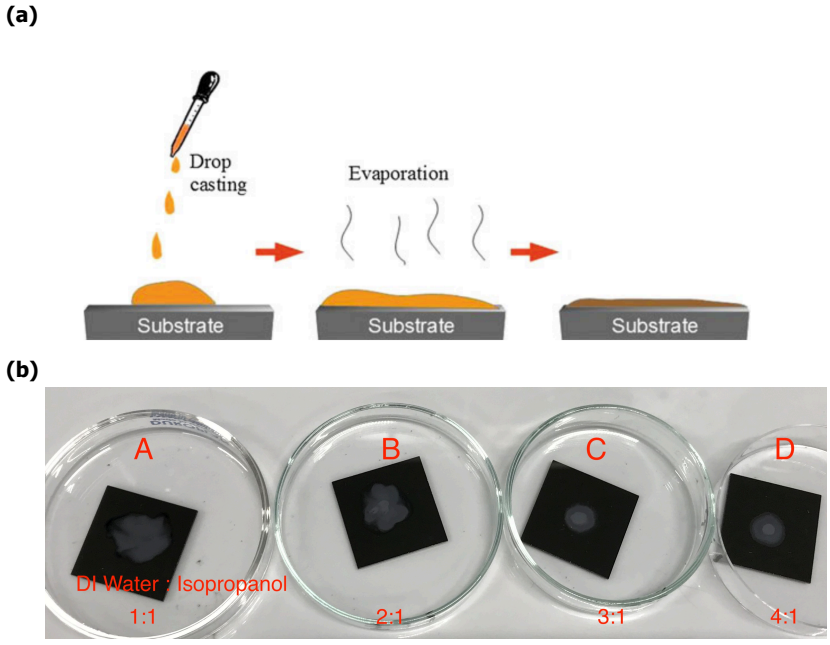

Figure 3.1: (a) Schematic illustration of the drop-casting technique. Adapted from [47]. (b) Drop-casted MoS_2 on glassy carbon plates with 4 different ink formulas

diffuse quickly on the substrate, making the quality of films difficult to control. To find out the optimised ink formula for glassy carbon substrates, four ink formulas with different water ratios to isopropanol were prepared and sonicated for 1 hour. After that, 50 μL of each ink was applied to glassy carbon plates by micropipette and left to dry at room temperature. The ink composition and results are shown in Tab. 3.1 and Fig. 3.1b, respectively. The ink tended to accumulate and flow slower with increasing DI water ratio because of the hydrophobic nature of glassy carbon. An appropriate ratio of water to isopropanol optimizes the uniformity of MoS_2 films. Since films made from formula C and D were more uniform than formula A and B, the ink formula applied to glassy carbon plates was decided to be 100 μL Nafion, 700μL DI water, and 200 μL isopropanol.

Table 3.1: Four different ink formulas for drop-casted MoS_2 on glassy carbon plates.

Formula	**A**	**B**	**C**	**D**
MoS_2 nanopowder (mg)	4	4	4	4
Nafion (μL)	100	100	100	80
DI Water (μL)	450	600	675	800
Isopropanol (μL)	450	300	225	200
DI Water/Isopropanol	1:1	2:1	3:1	4:1

The optimized ink formula needs to be adapted for different types of substrate. The ink used to drop-casting on germanium crystals contained 4 mg MoS_2 nanopowder, 20 μL Nafion, 240 μL DI water, and 480 μL isopropanol. The reduced Nafion ratio decreased the possibility of film peeling during ATR-FTIR experiments.

3.2. Electrochemical Measurements

The principles and aims of performing cyclic voltammetry, chronoamperometry, and SVET are described in this section.

3.2.1. Cyclic Voltammetry (CV)

Cyclic Voltammetry (CV) is a widely used potential sweep electrochemical technique to study the activity of electrocatalysts. A CV experiment was conducted by linearly sweeping the working electrode potential across a range and then returning to the initial potential. During the potential sweep, the resulting current, associated with the catalyst activity, was measured. The repeated CV cycles could offer insight into the stability of catalysts. Therefore, cyclic voltammetry in this work was applied to examine the activity and the stability of tested electrocatalysts. A VSP-300 (Biologic) potentiostat was used to perform CV and CA experiments. The setup used for the experiments is shown in Fig. 3.2. The working electrode was connected to the potentiostat by copper tape and covered by non-conductive tape except an exposed circular area with a 4 mm diameter. All CV experiments were performed at the scan rate of 20 mV s^{-1} except for the stability test of 100 CV cycles, where the applied scan rate was 50 mV s^{-1}.

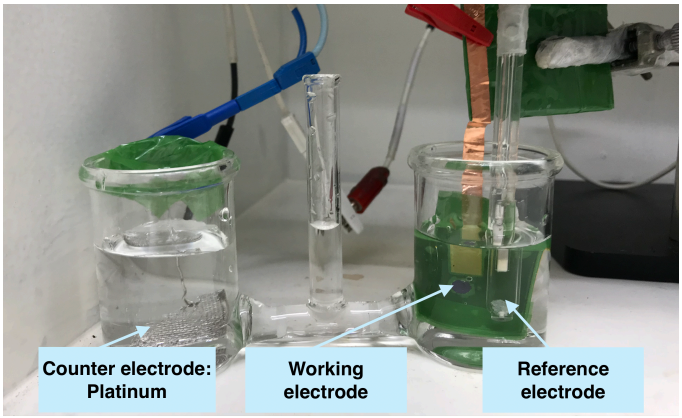

Figure 3.2: The H-cell setup for CV and CA experiments.

3.2.2. Chronoamperometry (CA)

Chronoamperometry is a time-dependent electrochemical technique where a constant applied potential is applied to the working electrode and the resulting current is measured versus time. The aim of using CA in this thesis was to investigate the stability of electrocatalysts.

3.2.3. Scanning Vibrating Electrode Technique (SVET)

The scanning vibrating electrode technique (SVET), a localized electrochemical technique, has been used in corrosion research, such as galvanic corrosion, inorganic coatings, and painted metals for 30 years; however, its use is still restricted to some research groups. SVET is considered a tool to visualize electrochemical processes by providing the distributions of local ionic current density in the solution above the sample of interest. Figure 3.3a displays typical current density maps measured at the extreme of the vibrating electrode probe. Making the electrode vibrate can reduce noise significantly, leading to a high signal-to-noise ratio. Thus, the measured current is more closed to the theoretical one. Truly quantitative information still relies on modeling tools [48]. The principle of SVET measurement is illustrated in Fig. 3.3b. When the probe vibrates in the solution (resistive element), a potential difference is detected, which can be further converted into current density via Eq. 3.1.

$$I = \frac{E}{\rho} = \frac{\Delta V}{\Delta r} \tag{3.1}$$

Where ρ is the resistivity of the solution, E is the electric field in solution, and ΔV is the potential difference between two points separated by the distance Δr in the direction of current flow [48].

According to DFT calculations, the edge of MoS_2 is more active; however, this has not been demonstrated by in-situ experiments. Besides, SVET has not been utilized for CO_2RR study to date. The aim of using SVET (Applicable Electronics) in this study is thus to investigate if SVET can be used in CO_2RR research and examine the activity of the MoS_2 edge.

Three different types of samples were employed for SVET measurements. To fabricate the first type of sample, a special cleanroom tape (Ultratape) was used to mechanically exfoliate bulk MoS_2 (HQ Graphene) to a few layers, which was then transferred to Si/SiO_2 wafer (MicroChemicals GmbH). The second sample was CVD-grown MoS_2 on a silicon wafer received from the University of Groningen. The third one was drop-cased MoS_2 on glassy carbon and the fabrication method has been

(a)

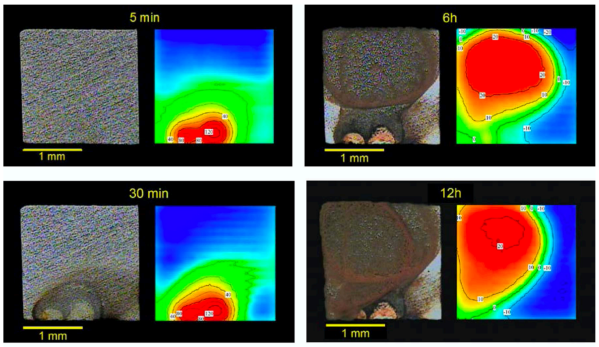

(b)

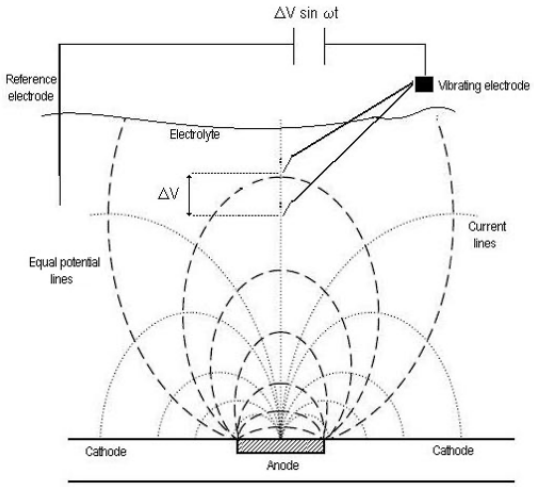

(c)

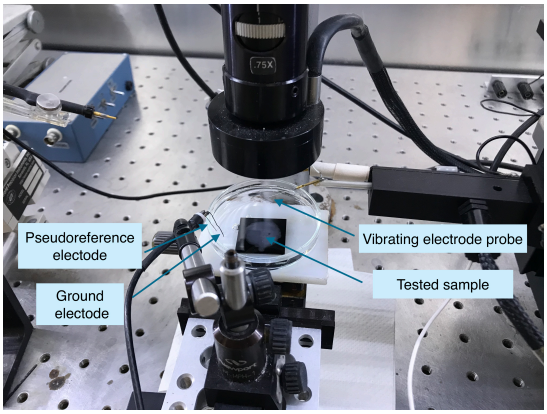

Figure 3.3: (a) Typical maps of current density measured by SVET. Blue color indicates negative (cathodic) currents while red one presents positive (anodic) currents. Adapted from [48]. (b) Schematic representation of the SVET working principle. Adapted from [49]. (c) The experimental setup of SVET.

mentioned in section 3.1. Figure 3.3c shows the setup for SVET. The electrode probe was calibrated and vibrated about 150 μm above the sample surface in the CO_2-saturated 0.1 M $KHCO_3$ electrolyte.

3.3. CO_2 Reduction Product Analysis

Gas chromography and ATR-FTIR are selected to analyze CO_2RR products. Their working principles and experimental setups are briefly described in this section.

3.3.1. Gas Chromography (GC)

Gas chromatography (GC) is an analytical technique that can separate a mixture of volatile components and then classify them quantitatively. A schematic of a GC system is shown in Fig. 3.4a. Once products are injected into a GC system, they are moved through the column by a carrier gas, which is the mobile phase. The separation of the product mixture occurs in the column coated with a stationary phase because each compound travels at its own speed depending on its interaction with the stationary phase. Detectors are connected to the column exits in order to sense the separated compounds [50].

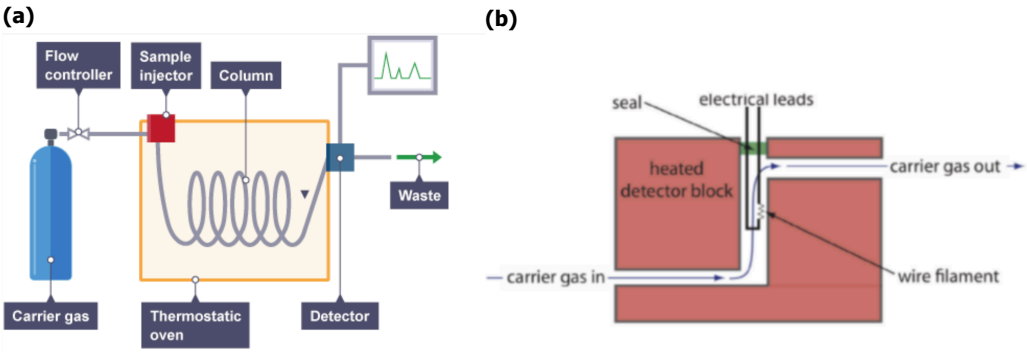

Figure 3.4: (a) The basic components in a GC system. Adapted from [51]. (b) Schematic diagram of a thermal conductivity detector showing one cell of a matched pair. The sample cell takes the carrier gas as it elutes from the column. A source of carrier gas that bypasses the column passes through a reference cell. Adapted from [52].

The gas chromatography utilized in this study is CompactGC4.0 (GAS). Three separate columns are used simultaneously in the system, enabling to detect most of the gaseous products. The first column is connected to a flame ionization detector (FID), which relies on differences of boiling point/vapor pressure differences to detect products. The second and third columns are linked to thermal conductivity

detectors (TCD). This detection is based on the comparison of the carrier gas as a reference and the mixture of carrier gas and gaseous products. Carrier gas should have a high thermal conductivity so that the temperature difference could be maximized. When an analyte elutes from the column, the thermal conductivity of the mobile phase in the TCD sample cell decreases, and the temperature of the wire filament increases, and thus the resistance also increases (Fig. 3.4b). On the other hand, a reference cell, through which only the carrier gas passes, can be used to correct time-dependent variations such as flow rate, pressure, and electrical power [52]. All compounds have a different thermal conductivity from helium except H_2, which makes TCD a good general purpose detector for initial investigations with an unknown sample [53]. Nevertheless, FID is sensitive mainly to hydrocarbon products. The difference between the two separate TCD columns is the use of carrier gas. TCD-1 connected to the second column utilizes He as the carrier gas in order to measure O_2 and CO, whereas it is difficult to quantify H_2 with He as carrier gas due to their similar thermal conductivity properties. In TCD-2 linked to the third column, Argon (Ar) is used as the carrier gas for detecting H_2 concentration. However, TCD-2 is insensitive for O_2 identification because Ar and O_2 have comparable thermal conductivity values. The product selectivity of catalysts can be determined by choosing proper detectors and types of carrier gases in a GC system.

In this research, the expected products are CO and H_2, thereby the detection limit of TCD affects the product selectivity analysis of the selected catalysts. Although TCD can defect a great number of products by using the non-destructive method, a significant drawback for TCD is its poor detection limit, which is ranged between 10 and 100 ppm[53–55].

The electrochemical cell used for GC measurements is similar to the design depicted in Fig. 2.1b, but the working electrode was changed to glassy carbon coated with MoS_2 film. CO_2 gas flowed into the cell with a rate of 8 ml/min. The electrolyte used was 1.8 mL of 0.1 M $KHCO_3$, which was saturated for 15 mins with CO_2 prior to GC measurements.

3.3.2. ATR-FTIR

Attenuated total reflectance - Fourier transform infrared spectroscopy (ATR-FTIR) is a surface-sensitive technique to in situ monitor chemical reactions and probe reaction intermediates [56, 57]. Unlike the transmission method requiring infrared (IR) beam to go through the sample, ATR is an internal reflection-based approach. In ATR-FTIR spectroscopy, the tested sample is supported by the ATR crystal. The IR beam passes through the crystal and interacts with the sample only at the point where the total internal reflection occurs. ATR crystals materials must have a refraction index that is higher than that of the tested sample so that the total internal reflection can be obtained. Germanium is commonly used as ATR crystals because

of its high refraction index. At the reflection point, the so-called evanescent waveforms and extends into the sample as illustrated in Fig. 3.5a. Depending on the composition of the sample, specific parts of the IR light are absorbed during the interaction between the evanescent wave and the sample, leading to a slightly attenuated total reflection [57].

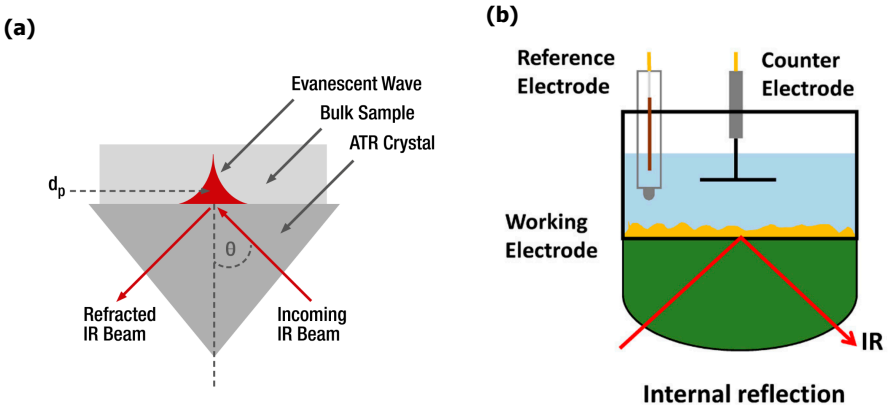

Figure 3.5: Schematic illustration of (a) the ATR-FTIR working principle (Adapted from [57]) and (b) ATR-FTIR cell (Adapted from [58]).

The penetration depth, which indicates how far the evanescent wave stretches into the sample, is dependent on the wavelength of incident light. The effective path length of the ATR crystal is also affected by the incident wavelength because it is defined by the number of internal reflections multiplied by the penetration depth of the evanescent wave. In the case of transmission/absorbance cell, the path length remains the same for each wavelength. Therefore, the intensity of the individual bands in the spectrum measured with the ATR cell is different from that of the transmission/absorbance spectrum. However, the position of the peaks shown in the ATR spectrum and the transmission/absorbance spectrum is similar [56]. By using ATR-FTIR, adsorbed species on catalysts are revealed.

The accessory used for the ATR-FTIR experiments in this study is the VeeMAX III and the electrochemical cell is similar to the setup in Fig. 3.5b. The used ATR germanium crystal was coated with the MoS_2 ink, whose formula has been mentioned in section 3.1.

3.4. Surface Characterisation

SEM, EDS, and XPS were performed to characterize the electrocatalyst materials. Their working principles are briefly explained in this section.

3.4.1. Scanning Electron Microscopy (SEM)

SEM is a technique that scans the sample surface with a focused beam of electrons interacting with atoms at the sample surface. The interaction produces various signals revealing information about the morphology and composition of the sample surface [59].

SEM provides higher resolutions than optical microscopes. The resolution of microscopy is limited to half of the wavelength of the incident beam [60]. Conventional optical microscopes use visible light whose minimum wavelength is 400 nm, which means that a smaller than 200 nm object can not be seen by a light microscope [61]. According to the de Broglie wave equation, the momentum of a particle determines its wavelength. By controlling accelerating voltages, a much shorter wavelength of electrons than that of photons is achieved, contributing to the high resolution of SEM. The SEM (JSM-IT100) equipped with a JEOL-made EDS was used to study the morphology of tested samples in this work.

3.4.2. Energy-Dispersive X-ray Spectroscopy (EDS)

Energy-dispersive X-ray spectroscopy (EDS) is a qualitative and quantitative technique for elemental analysis. When the primary electron beam knocks off an electron from the inner low-energy shell, an electron-hole is generated. Another electron from the outer high-energy shell is then attracted to fill the vacancy, which causes the emission of a characteristic X-ray. The specific energy of the X-ray can be used to identify elements present in the sample [62]. However, users should be aware of that some elements have overlapping peaks; thereby, automated identification of peaks are not always reliable. Besides, characteristic X-rays are generated in a region about 1-3 μ deep, depending on the accelerating energy and materials, etc., which makes EDS not a true surface-analysis technique [63].

3.4.3. X-ray Photoelectron Spectroscopy (XPS)

X-ray photoelectron spectroscopy (XPS) is one of the most used techniques to analyze the sample surface, capable of obtaining information on the chemical composition (atomic percentage) and the oxidation state of a sample on a selected area of the surface [59]. An XPS spectrum is obtained by irradiating the sample with an X-ray beam and measuring the energy of the emitted electrons from the sample surface. The primary advantages of using the XPS technique are simple sample preparation, rapid measurement, detailed chemical bonding identification, and its use as a complementary technique to other typical characterization techniques, i.e., TEM, SEM, XRD, and EDS.

XPS analysis was conducted by a PHI-TFA XPS spectrometer (Physical Electronic Inc.), equipped with an x-ray Al-monochromatic source. The vacuum during XPS analysis was 10^{-9} mbar. The investigated area was 0.4 mm in diameter, and the analysis depth was 3-5 nm. Narrow multiplex scans of the peaks were collected using a pass energy of 23.5 eV with a step size of 0.1 eV at a take-off angles of 45° with respect to the sample surface. A low energy electron gun was utilized for surface charge neutralization XPS. Spectra were evaluated with Multipak v8.0 (Physical Electronics Inc.).

4

Results and Discussion

This chapter presents and discusses the results of CO_2RR experiments using MoS_2 as a catalyst. MoS_2 catalytic performances in terms of current density, product selectivity, and stability are discussed. This is followed by a discussion about the results of catalyst characterization.

4.1. Electrochemical Measurements

Current Density

The activities of selected catalysts were examined by cyclic voltammetry. The correlation between applied potential and measured current density was recorded in voltammograms. As a commonly used electrolyte, CO_2-saturated potassium bicarbonate ($KHCO_3$) solution can quickly neutralize the local OH^- ($HCO_3^- + OH^- = CO_3^{2-} + H_2O$) and reduce the local pH [64]. To obtain insight into the effect of $KHCO_3$ concentration on the activity of MoS_2, CV experiments were performed on GCE coated with MoS_2 film in different concentration of $KHCO_3$ solution purged with CO_2 (0.1M, 0.5M, and 1M) at the sweep rate of 20 mV s^{-1}. Each experiment was carried out independently. Figure 4.1a shows the current density of the sample became larger with increasing $KHCO_3$ concentration. The reason behind this can be that the conductivity of the electrolytes were enhanced with increasing $KHCO_3$ concentration. However, the drop-casted MoS_2 films were removed easily in high concentration of $KHCO_3$ solution, which might be caused by the formation of numerous bubbles on the electrode surfaces at highly negative potentials. Besides, the previous study has indicated the Faradaic efficiency of CO_2 reduction decreases with increasing $KHCO_3$ concentration because large quantities of K^+ are attracted to the cathode, blocking the adsorption of CO_2 on the cathode. Based on above two reasons, 0.1M $KHCO_3$ solution was more suitable than 0.5M and 1 M for CO_2

reduction experiments [65].

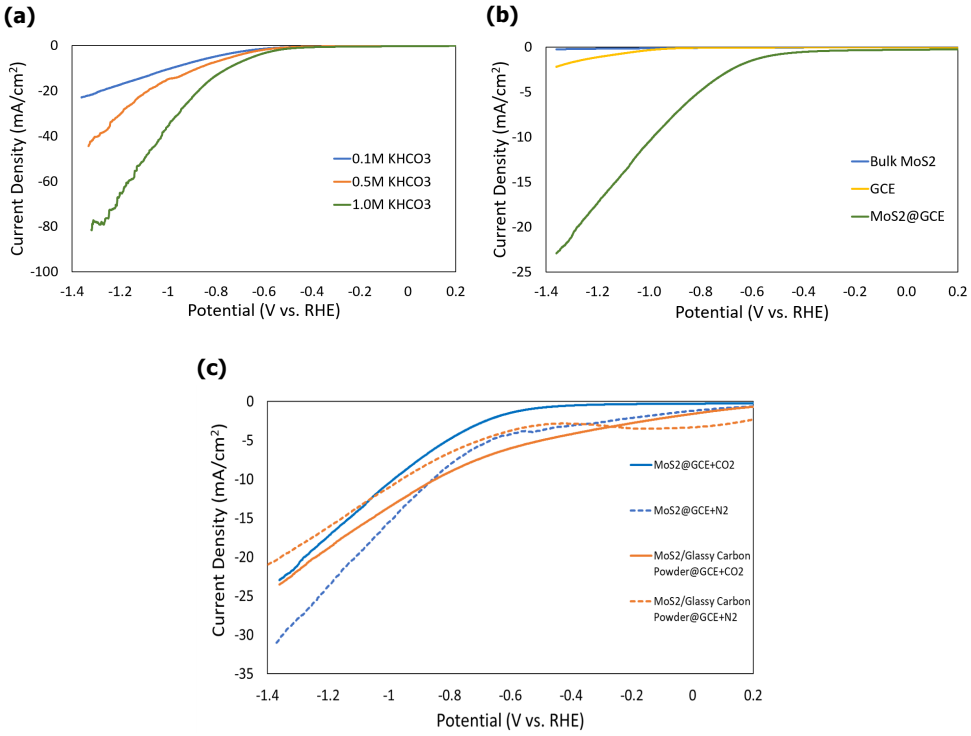

Figure 4.1: (a) CV curves of drop-casted MoS_2 on GCE in CO_2-saturated aqueous solution mixed with different $KHCO_3$ concentration. (b) CV curves of bulk MoS_2, bare GCE and drop-casted MoS_2 on GCE in CO_2-saturated 0.1M $KHCO_3$ aqueous solution. (c) CV curves of MoS_2@GCE and MoS_2 mixed with glassy carbon powder@GCE in CO_2-saturated (solid line) and N_2-saturated (dashed line) 0.1M $KHCO_3$ aqueous solution.

As Fig. 4.1b shows, GCE modified with MoS_2 film exhibited much higher activity than bare GCE and bulk MoS_2 in CO_2-saturated 0.1M $KHCO_3$ aqueous electrolyte (pH=6.7). The current density of bulk MoS_2 was the lowest among them. The reduction current density of GCE even exceeded that of bulk MoS_2 at around -1.0V vs. RHE. Two possibilities made the differences in the reduction current density between bulk MoS_2 and drop-casted MoS_2. One possibility was related to the exposed area in the electrolyte. The porous structure of drop-casted MoS_2 revealed in Fig. 4.8b allowed the larger exposed area. Besides, the MoS_2 film consisting of nanopowder contributed to a larger surface than the bulk MoS_2 with a laminar structure. The other possibility was due to the low conductivity of bulk MoS_2, leading to the difficulty in transporting charge between the resistive electrode and active sites. The dependence of electrocatalyst activity on its conductivity was thus investigated. The conductivity of drop-casted MoS_2 films on GCE was enhanced by adding 1.5 mg glassy carbon powder (GCP) to the formula mentioned in section 3.1.

GCP was chosen because of its high conductivity and electrochemically inert nature. Compared with MoS_2 films, the current densities of MoS_2/GCP films were always larger in CO_2-saturated 0.1M $KHCO_3$ solution over the range of tested potentials (Fig. 4.1c). However, this was not the case under the N_2-saturated condition. This was likely due to the presence of glassy carbon powder on the film surface, which reduced MoS_2 coverage and led to a lower HER rate.

Figure 4.2a displays voltammograms carried out in CO_2-saturated ionic liquid-based aqueous electrolyte consisting of 4 mol% [EMIM]-[BF_4] and 96 mol% deionized water (pH=4). MoS_2@GCE shows a reduction peak which could be related to CO_2 reduction [66]. Bulk MoS_2 had a much better catalytic performance for CO_2RR in the ionic liquid-based solution than in 0.1M $KHCO_3$ aqueous solution. It was discovered that $[EMIM]^+$ cations can bind to CO_2, forming a complex of $[EMIM{-}CO_2]^+$ which is stable in an acid environment. The $[EMIM{-}CO_2]^+$ complexes tend to be physisorbed at the negatively charged MoS_2 cathode by Coulombic and van der Waals coupling, which reduces the reaction barrier for electrons transporting through CO_2, resulting in the enhanced catalytic performance of bulk MoS_2 [27, 67]. Another significant improvement in catalytic activity can be seen on the MoS_2@GCE samples which had been exposed to CO_2-saturated 0.1M $KHCO_3$ with constant negative potentials applied for 1 hr Fig. 4.2b. The interpretation of this phenomenon will be discussed in subsection 4.3.2. Although better catalytic performance for CO_2RR could be achieved in the ionic liquid-based electrolyte, the MoS_2 films delaminated rapidly in the solution.

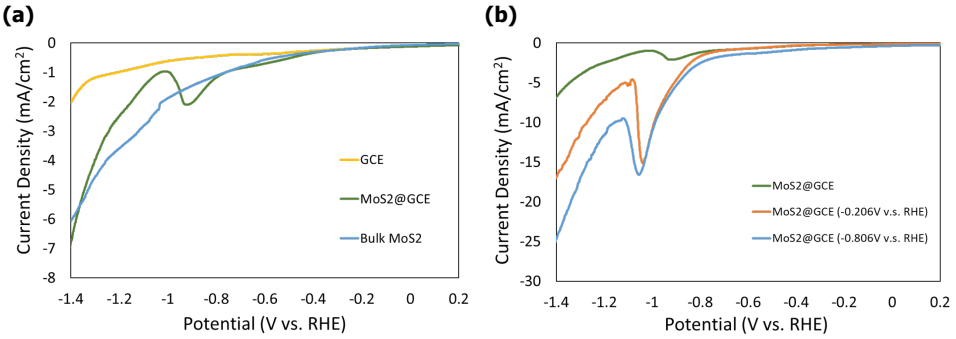

Figure 4.2: (a) CV curves of bulk MoS_2, bare GCE, and drop-casted MoS_2 on GCE in CO_2-saturated ionic liquid-based solution (96 mol% deionized water and 4 mol% [EMIM]-[BF_4]). (b) CV curves of drop-casted MoS_2 samples in CO_2-saturated ionic liquid-based solution (96 mol% deionized water and 4 mol% [EMIM]-[BF_4]). Orange and blue indicated the samples that had been immersed in CO_2-saturated 0.1M $KHCO_3$ at -0.206 V vs. RHE and -0.806 V vs. RHE respectively for 1hr.

Catalyst Stability Evaluation

Stability is an essential criterion for catalyst selection. The stability of the MoS_2 film was tested with CV and CA measurement. The comparison of 1^{st} and 100^{th} CV

cycles presented in Fig. 4.3a indicates the good stability of drop-casted MoS_2@GCE after 100 CV cycles in spite of the existence of small differences resulted from the continuous purging of CO_2 gas into the electrolyte altering the distance between the working electrode and reference electrode and thus changing the resistance of the system. Furthermore, the bubbles generated on the electrode surface also influence the measurements. Attached bubbles masking the electrode surface decrease the effective electrocatalytic area, while detached and free bubbles could interfere with current transport by blocking possible ion pathways. The formation and detachment of bubbles lead to fluctuations of the curves [68].

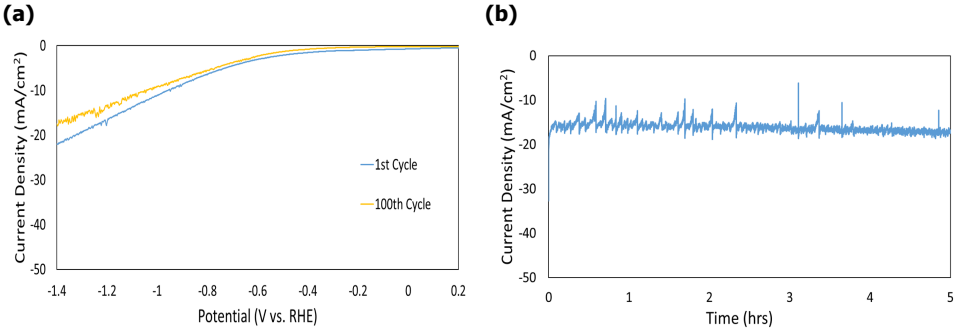

Figure 4.3: (a) Cyclic voltammograms of MoS_2@GCE before and after 100 cycles at a scan rate of 50 mV s^{-1}. The potential was swept from +1.14 to -1.56V vs. RHE. (b) Chronoamperometry (CA) of MoS_2@GCE at -1.2 V vs. RHE in CO_2-saturated 0.1M $KHCO_3$ electrolyte for 5 hours.

The chronoamperometry experiment was performed on MoS_2@GCE in the 0.1 M $KHCO_3$ solution at -1.2 V vs. RHE for 5 hours to test the stability of MoS_2 film. The results shown in Fig. 4.3b indicates the current density of drop-cased MoS_2 film remained stable and showed no decay for 5 hours.

Current Density Maps (SVET)

The distribution of local current density on selected catalyst surfaces was measured by SVET in CO_2-saturated 0.1 M $KHCO_3$ under an open-circuit condition. The results reveal that the detection of thin MoS_2 films is possible. The MoS_2 flakes exfoliated from bulk MoS_2 were first measured in a dark environment. The reduction current pattern in the center after 15 minutes of immersion in Fig. 4.4a was presumably due to MoS_2 flakes based on the shapes, although the position was slightly shifted. Considering the SVET set-up depicted in Fig. 4.4b and the size of flakes, the shifting is reasonable. The vibrating probe of SVET did not scan on the film surfaces in solution, but 150 μm above it. Besides, the estimated diameter of the platinized SVET probe is between 15-20 μm. To be detected by SVET, the dimension of flakes should be larger than 100 μm, which is difficult to reach by physical exfoliation. Furthermore, MoS_2 edges are considered to be active sites based on DFT calculation, which can not be demonstrated by SVET due to the limitation of SVET probe

dimension.

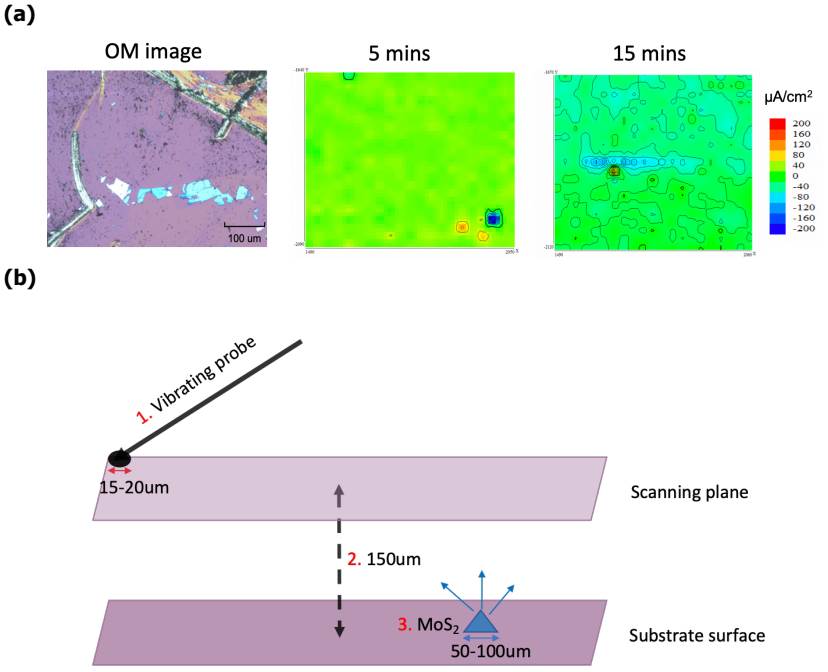

Figure 4.4: (a) SVET measurement of exfoliated MoS_2 flakes on Si/SiO_2 wafer during the first 15 minutes of immersion in CO_2-saturated 0.1 M $KHCO_3$ under the dark condition. Current density is recorded in the unit of μA cm^{-1}. Negative values indicate cathodic currents (blue) and positive ones are anodic currents (red). (b) Schematic illustration of SVET set-up.

CVD-grown MoS_2, which exhibited a large area of a few-layer MoS_2, was also tested. The maps of local current density obtained under blue light irradiation (450 nm wavelength) are represented in Fig. 4.5a. In the first 5 minutes, the area of monolayer MoS_2 showed stronger cathodic activity than the Si/SiO_2 substrate and multi-layer MoS_2. However, the intensity of cathodic current measured on the monolayer MoS_2 decreased gradually with time and disappeared in the 15 minutes. From then, the observed anodic current dominated the right part and spread out to the left side. The cathodic current in the first 5 minutes could be caused by the photocatalytic CO_2 reduction over the MoS_2 monolayer. The detected reduction current decreased with depletion of CO_2 concentration in the electrolyte and eventually became zero in 15 minutes. The photocatalytic performance of MoS_2 is related to its thickness-dependent bandgap structure. The bandgap of MoS_2 increases with the thickness decreasing. The bandgap structure turns from the indirect to direct bandgap when the monolayer is reached, resulting from quantum confinement effects [69]. An earlier study also indicated the photocatalytic activity of MoS_2 was enhanced dramatically with decreasing its layer-number [70]. The film in the chosen area was removed after cleaned with deionized water, isopropanol and acetone; therefore, the performance under the dark condition could not be conducted. The

comparison between dark and light illumination needs further investigation.

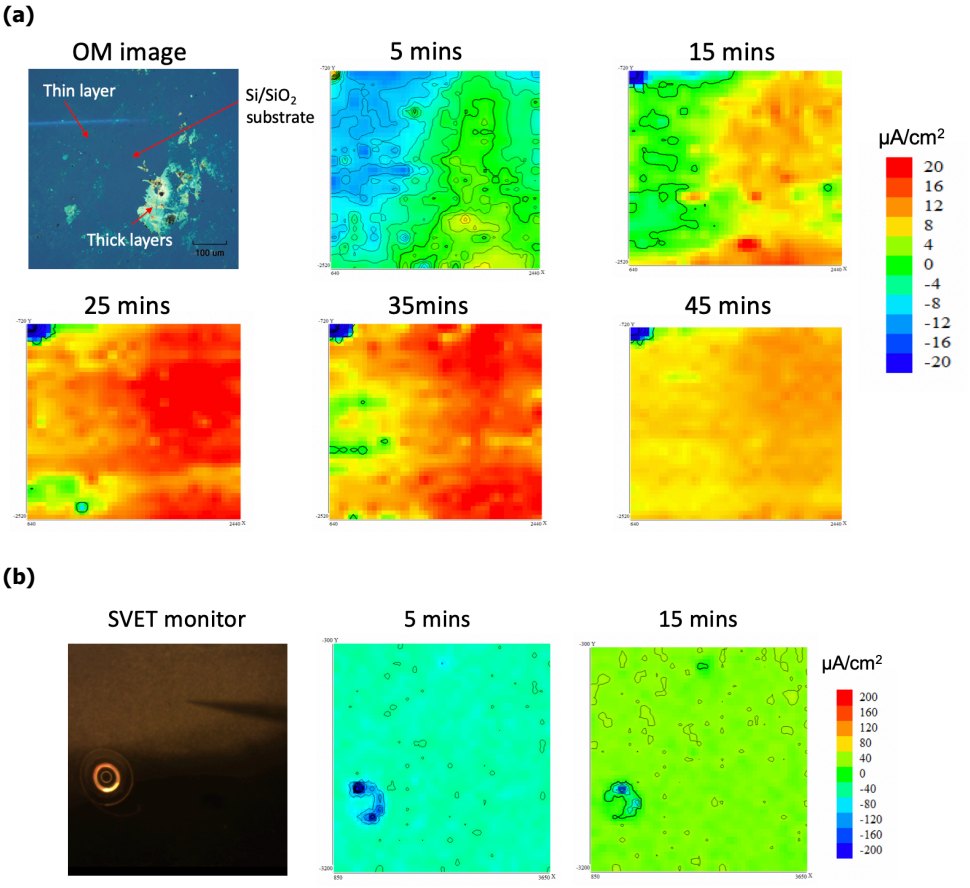

Figure 4.5: (a) SVET measurement of CVD-grown MoS_2 flakes on Si/SiO_2 wafer during the first 45 minutes of immersion in CO_2-saturated 0.1 M $KHCO_3$ under blue-light illumination. (b) SVET measurement of drop-casted MoS_2 films on GCE during the first 15 minutes of immersion in CO_2-saturated 0.1 M $KHCO_3$ in dark environment.

The third SVET measurement was conducted on drop-casted MoS_2 coated on GCE in a dark environment. There was no current density difference seen between drop-casted MoS_2 and the glassy carbon substrate in Fig. 4.5b, while the other two samples showed the difference with the substrates. This implies that the activity of drop-casted MoS_2 might be lower than exfoliated MoS_2 and CVD-grown MoS_2. Additionally, it should be aware that bubbles on the sample surfaces affected the measurements by interfering with the vibrating probe. The generation of bubbles in CO_2-saturated electrolyte is unavoidable, resulting in the operation difficulty in using SVET for CO_2RR experiments.

4.2. Product Analysis

Gas chromatography (GC) was performed to investigate catalytic selectivity of MoS_2 @GCE in CO_2-saturated 0.1M $KHCO_3$. Figure 4.6 shows no product detected at -0.206 V due to the low reaction rates and 98.4% FE of H_2 evolution at -0.806 vs. RHE. The 1.6 FE% loss was attributed to CO formation, although the CO concentration was too low to be quantified by GC. As mentioned in subsection 3.3.1, product concentration below the range of 10-100 ppm is challenging to be detected by the thermal conductivity detector in the GC system. The electrochemical cell used for the GC system was different from CV, which could contribute to differences in product selectivity. The GC cell with a high surface-to-volume ratio depletes dissolved CO_2 quickly, and the concentration of CO_2 in the cell is also susceptible to bubble sizes of purged CO_2 that affect gas to liquid CO_2 mass transfer [18]. These factors causing difficulties in maintaining the saturation of CO_2 in the GC cell might have suppressed CO production in GC measurements. Additionally, there was an initial charging period at the beginning displayed in Fig. 4.6a, which was due to the high porosity of the catalyst film according to earlier work, after which the current stabilized [71]. Based on the GC measurement results, MoS_2 film in aqueous media favorably catalyzed H_2 evolution, which is in agreement with the previous study [44, 72].

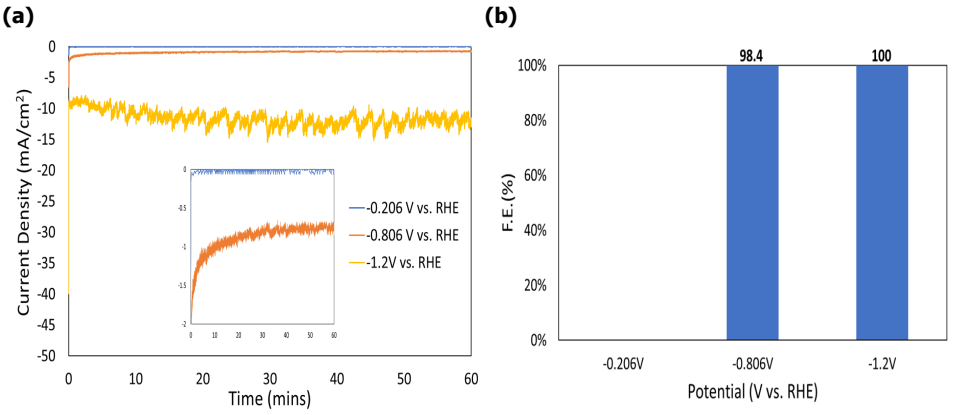

Figure 4.6: (a) Chronoamperogram and (b) calculated Faradaic efficiencies for CO_2RR products after 1 h potentiostatic electrolysis at -0.206, -0.806, and -1.2 V vs. RHE over two repetition.

FTIR spectra were collected continuously in order to study reaction intermediates during polarizing drop-casted MoS_2 film on the germanium crystal from +0.6 V to -1.8 V vs. RHE in CO_2-purged solutions. Figure 4.7a shows the comparison between the bare germanium crystal and the MoS_2 film coated on a germanium crystal. The peaks at ~865 cm^{-1} and ~2342 cm^{-1} were assigned to be carbonate ions and CO_2, respectively [73, 74]. CO is often detected as a band between 2100

and 1900 cm^{-1} in CO_2-saturated bicarbonate-based solutions [74–76]. Peaks at 1941, 1967, and 1992 cm^{-1} might be due to the presence of CO since the intensities of the peaks increased during cathodic polarization (Fig. 4.7b). It can be seen from Fig. 4.1c that the cathodic current of MoS_2 film on GCE in the CO_2-saturated solution was notably smaller than in the N_2-saturated solution, suggesting that CO presence might poison the electrode surface and inhibited HER [77]. Furthermore, compared with the GC measurement performed at -0.206 V vs. RHE, no product was detected, indicating that the availability of electrogenerated CO should be below the detection limit of gas chromatography (10-100 ppm).

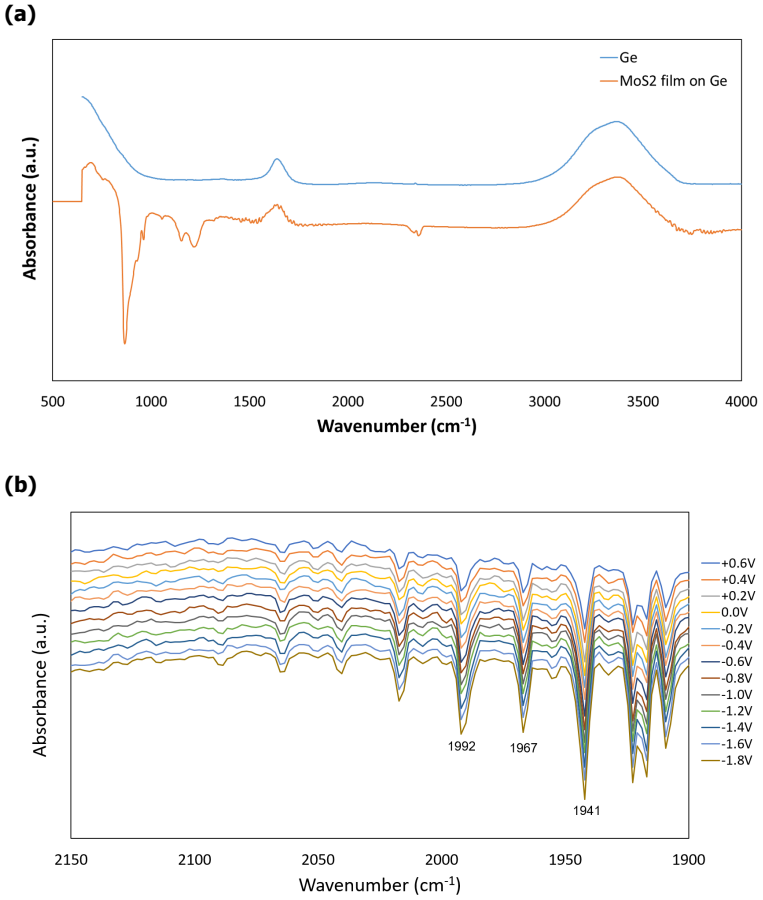

Figure 4.7: (a) In situ ATR-FTIR spectra of the germanium crystal and MoS_2 film coated on a germanium crystal in CO_2-saturated 0.1 M $KHCO_3$ under the OCP condition. (b) In situ ATR-FTIR spectra of CO generated in CO_2-saturated 0.1 M $KHCO_3$ when the potential was stepped in 0.2 V increments from +0.6V to −1.8 V vs. RHE on a MoS_2 film electrode. Spectra shown were 32 co-added scans at a 4 cm^{-1} resolution.

4.3. Surface Characterization

Characterization results of selected catalysts obtained by SEM, EDS, and XPS are presented and discussed in this section.

4.3.1. Morphology & Elemental Analysis

Figure 4.8a reveals that the stacked-layered structure of crystalline bulk MoS_2 and its morphology is significantly different from that of drop-casted MoS_2 film showing the highly porous structure displayed in Fig. 4.8b. This porous-network type morphology is beneficial for electrocatalysis because it allows all active sites within the film to be exposed to electrolyte [78]. In addition to the structure, MoS_2 nanopowder were uniformly distributed on glassy carbon plates.

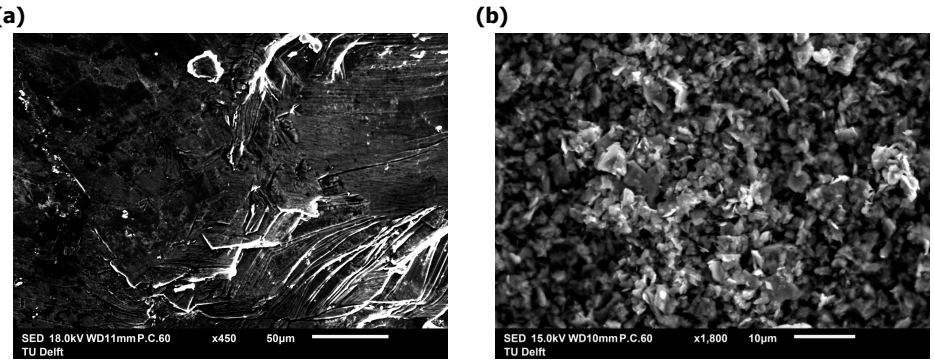

Figure 4.8: (a) SEM image of the bulk MoS_2 display its lamellar structure. (b) SEM image of drop-casted MoS_2 film shows the porous structure.

As Fig. 4.9a shows, there were many small cracks found in the MoS_2 film after the GC measurement (-0.806 V vs. RHE was applied to the MoS_2 @GCE for 1 hr in CO_2-saturated 0.1M $KHCO_3$ electrolyte). The EDS analysis result shown in Fig. 4.9c indicates the presence of potassium (K), carbon (C), fluorine (F), sulfur (S), and molybdenum (Mo). The detection of potassium was due to the use of $KHCO_3$ electrolyte. The standard reduction potentials for potassium ions is -2.93 V, which is much more negative than the applied potential; thereby, the K element detected by EDS can not be in the metallic form. It has been reported that the space between the S-Mo-S layers and the electrostatic stability of the negatively charged S^{2-} ions allow intercalation of alkali metals and even molecules [79–81]. Therefore, intercalation of K^+ ions in the MoS_2 film was speculated. K signals were still be detected after rinsed with DI water, indicating that it was not a simple deposition (Fig. A.2). Carbon detection was attributed to the glassy carbon plate while Mo and S signals were from MoS_2 nanopowder. The signal of fluorine came from the Nafion used as a binder in the drop-casted ink.

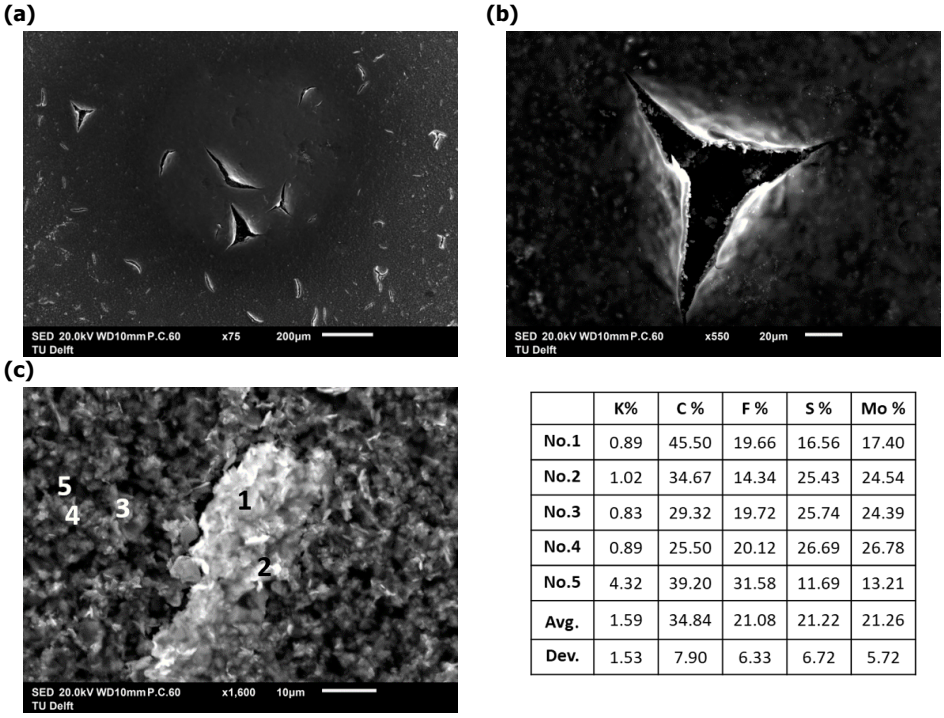

	K%	C %	F %	S %	Mo %
No.1	0.89	45.50	19.66	16.56	17.40
No.2	1.02	34.67	14.34	25.43	24.54
No.3	0.83	29.32	19.72	25.74	24.39
No.4	0.89	25.50	20.12	26.69	26.78
No.5	4.32	39.20	31.58	11.69	13.21
Avg.	1.59	34.84	21.08	21.22	21.26
Dev.	1.53	7.90	6.33	6.72	5.72

Figure 4.9: (a) (b) SEM images of drop-casted MoS_2 @GCE after the GC measurement (a constant potential of -0.806V vs. RHE was applied for 1 hour in CO_2-saturated 0.1M $KHCO_3$ solution).(c) EDS analysis of the MoS_2 film after the GC measurement.

Local detachment of MoS_2 films was also discovered on the sample used for the stability test of 100 CV cycles (Fig. 4.10a). The EDS elemental maps displayed in Fig. 4.10c confirm that the glassy carbon support in the detachment area was exposed. Formed oxide species could be SO_3, K_2O, and MoO_3 (see Fig. A.1 and Fig. A.2). It should be noted that Mo (L) signals were identified as Pb (M) due to the overlap between the Mo (L) and Pb (M) peaks (2.3 keV) in the EDS spectra [82, 83]. It is hypothesized that the detachment of MoS_2 films was caused by the interaction of bubble evolution and MoS_2 films. Nucleation of bubbles tends to occur on cracks in the electrode surface, and the bubbles grow by taking in gas from the dissolved gas boundary layer. When the buoyancy force overcomes the interfacial tension force, the bubbles detach from the electrode surface and induces convection in the liquid [68]. The friction generated during bubble growth and induced convection flow may account for the delamination of MoS_2 films.

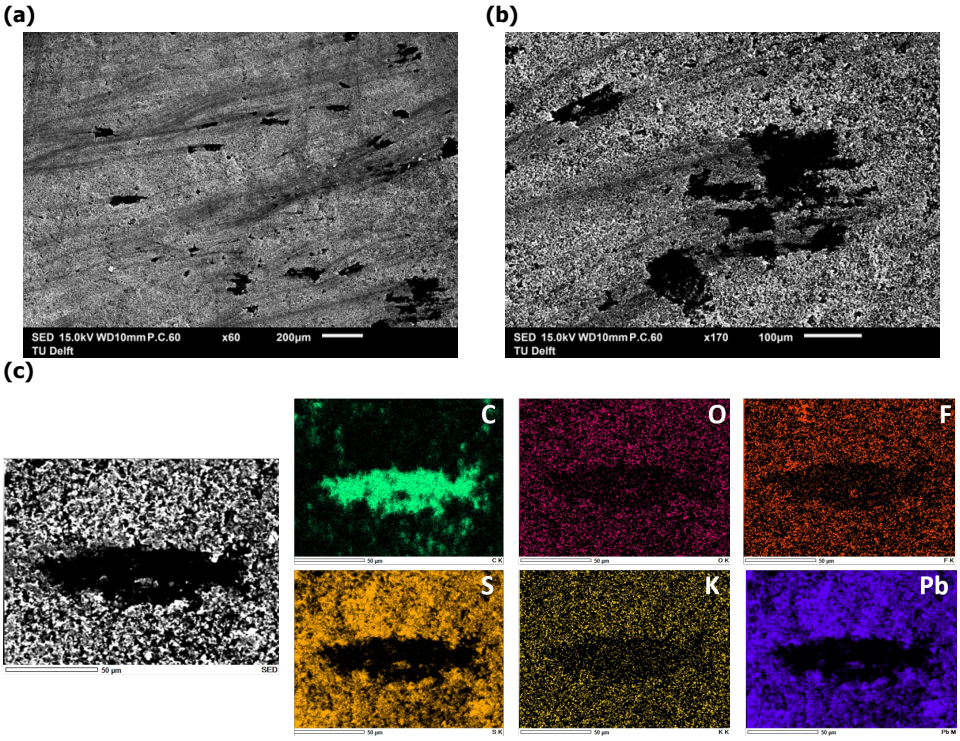

Figure 4.10: (a) (b) SEM images of drop-casted MoS_2 @GCE after 100 CV cycles in CO_2-saturated 0.1M $KHCO_3$ solution. (c) EDS elemental maps of MoS_2 @GCE after the stability test of 100 CV cycles.

4.3.2. Surface Analysis

X-ray photoelectron spectroscopy (XPS) was carried out to analyze the chemical components of the selected catalysts. Three samples were chosen: bulk crystal MoS_2, unexposed MoS_2@GCE, and exposed MoS_2@GCE which had been immersed in CO_2-saturated 0.1 M $KHCO_3$ at -1.0 V vs. RHE for 30 minutes.

The C 1s spectra (Fig. 4.11a) of all samples had a strong peak at 284.8 eV assigned to C–C species. The peak at 284.8 eV for bulk MoS_2 was likely to result from carbon contamination from the atmosphere [84]. The peak at ~294 eV for both MoS_2@GCE samples was assigned to CF_3 due to the presence of Nafion [84].

The peak of the O 1s spectrum (Fig. 4.11b) for bulk MoS_2 could be due to adsorbed oxygen (532 eV) [85]. There was a strong peak at ~533.2 eV in the oxygen spectrum of exposed MoS_2@GCE, but no peak was observed in that of unexposed MoS_2@GCE. Interpreting O 1s spectra is not straightforward since the O 1s binding energy of many compounds falls within a very narrow range, which makes O1s peaks tend to be broad with multiple overlapping components [86]. Both H_2O adsorption and CO adsorption could contribute to the observed oxygen peak on the exposed film [87, 88].

The Mo 3d spectra of bulk MoS_2 and unexposed MoS_2@GCE (Fig. 4.11c) show two peaks at ~232.2 and ~229.0 eV, which denoted Mo 3d3/2 and 3d5/2 with spin-orbit splitting energy of 3.2 eV attributed to Mo^{4+} oxidation state of MoS_2 [89]. A small peak at ~226.3 eV was because of S 2s. The Mo 3d5 peaks for the exposed MoS_2@GCE became much smaller than the other two samples. Two possibilities caused a decrease in Mo 3d5 signals. One of the possible reasons was a local detachment of MoS_2 films after the CA experiment. The other accounted for the change was the formation of oxide during CO_2RR covering the original MoS_2 films, supported by the O 1s spectrum. A similar phenomenon can be seen in the spectrum of S 2p3 (Fig. 4.11d) where the intensity of the sulfur signal significantly reduced on the exposed sample.

Due to the overlap of K 2p peaks and the CF_3 peak, the K 2s spectra (Fig. 4.11e) were checked. Only the spectrum of exposed MoS_2 film showed a peak, suggesting the presence of potassium on the MoS_2 film surface after the CA experiment, which is consistent with the EDS analysis presented in Fig. 4.9c. The peaks present in the F 1s spectrum (Fig. 4.11f) was attributed to the use of Nafion in drop-casted MoS_2 films.

The calculated values of E_f-E_{Vmax} shown in Fig. 4.12 suggest a notable change of bandgap structure in the exposed sample. The energy gaps between Fermi level and valence band maximum for bulk MoS_2 and the unexposed MoS_2 film were

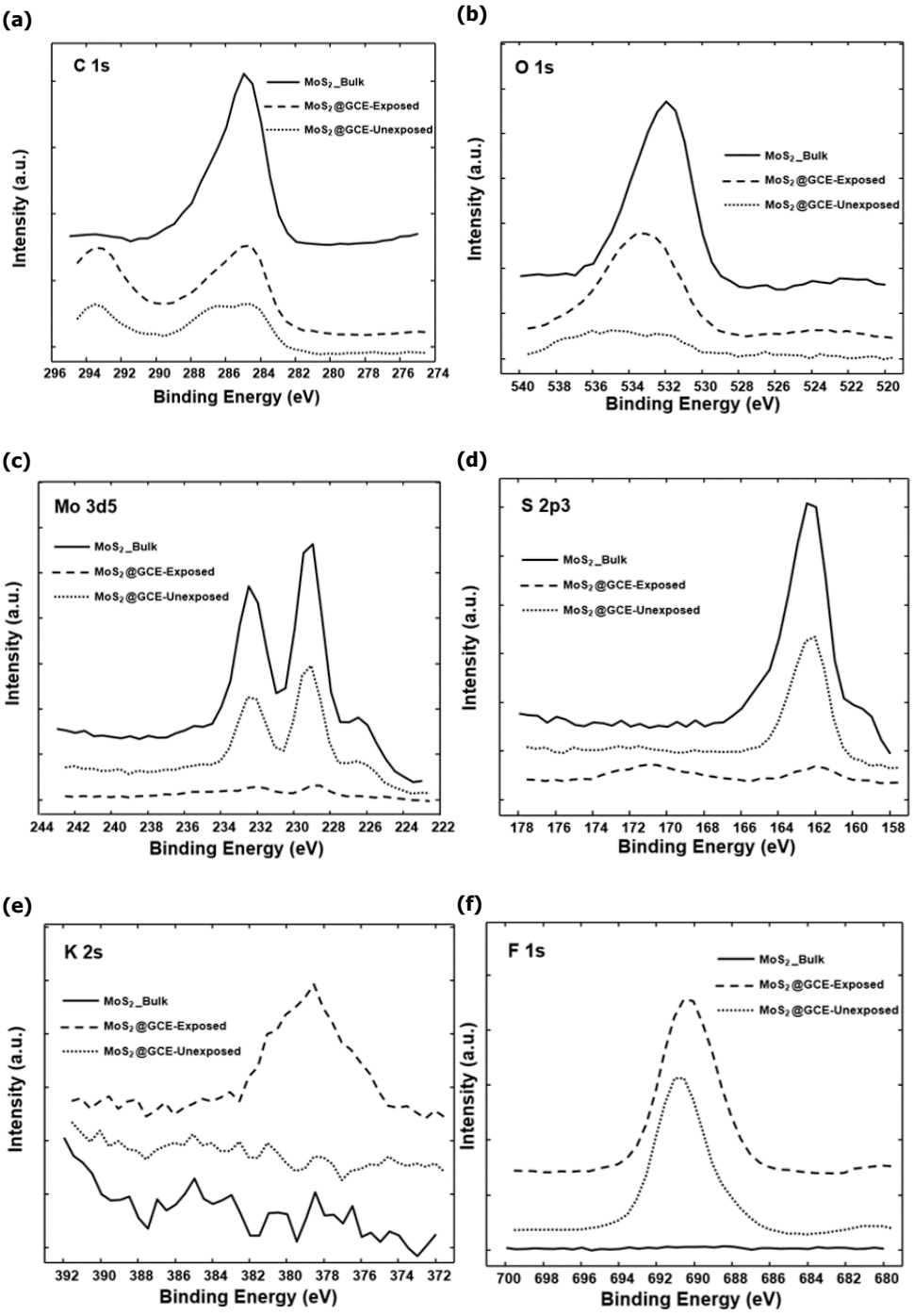

Figure 4.11: High-resolution XPS spectra for different forms of MoS_2.

0.238 eV and 0.271 eV. However, the gap for the exposed film dropped to 0.06 eV. It is hypothesized that the intercalation K^+ ions in the exposed MoS_2 film were responsible for the change of bandgap structure and electronic property. This might provide a reason for the improvements of catalytic activity observed on the exposed MoS_2 film in ionic liquid-based aqueous solutions (Fig. 4.2b).

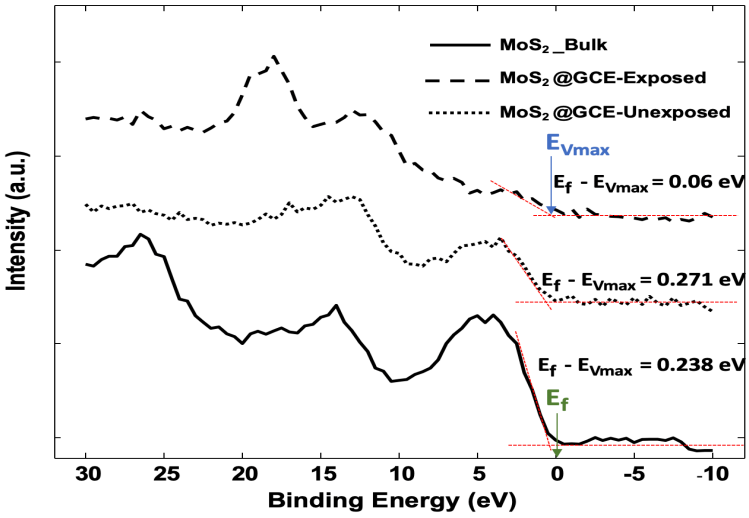

Figure 4.12: Valence-band spectra for different forms of MoS_2

5

Conclusion

This research aimed to investigate the electrocatalytic performance, i.e., activity, selectivity, stability, of MoS_2 for the electrochemical CO_2 reduction reaction (CO_2RR). It was discovered that the catalytic performance of MoS_2 film on the glassy carbon electrode dominates over the bulk form in aqueous solutions. The poor performance of the bulk MoS_2 could be ascribed to its low conductivity. In contrast, enhanced activity was observed on the MoS_2 film combined with glassy carbon power, indicating the importance of the electrical conductivity. Additionally, it was found that the fabricated MoS_2 film maintains its electrocatalytic reactivity for at least 5 hours monitored in this work. While MoS_2-based catalysts showed high product selectivity towards H_2 evolution in aqueous solutions, ionic-based liquids showed to be potential electrolyte candidates for CO_2RR. Furthermore, the enhanced CO2RR performance observed on the MoS_2 film with potassium incorporation indicates a route for improving its catalytic performance using potential dopants to tune its electronic properties, e.g., bandgap structure.

6

Future Outlook

Despite the extreme low product selectivity towards CO formation, the catalytic performance of MoS_2 films could be improved by tuning the bandgap structure of MoS_2 and modifying electronic properties. This study has demonstrated that the MoS_2 film with an adjusted bandgap structure exhibited better activity in the ionic liquid-based solution. The literature also reported that Cu/MoS_2 composite with enhanced electronic conductivity showed a remarkably higher CO formation rate than pure MoS_2 [72]. In addition, integrated three-dimensional $TiO_2@MoS_2$ and niobium-doped MoS_2 displayed superior CO Faradaic efficiency [14, 44]. Both doping and co-catalyst are effective ways to increase CO_2RR product FE% of MoS_2.

Regarding the experimental methods, setups, and results, the limitations such as low durability of drop-casted MoS_2 in the ionic liquid-based solution and low solubility of CO_2 could be enhanced by the following suggestions. (1) Evaporation of Nafion during sonification lowers the durability of drop-casted MoS_2 film. Sonification of the drop-casting ink in an iced bath could reduce the evaporation rate. (2) The composition of drop-casting ink for germanium crystal should be further optimized to prevent film delamination during polarization. (3) Gas diffusion electrodes could also be used to overcome the low solubility of CO_2. (4) Deconvolution of the existing XPS spectra can provide a better understanding of the surface change.

The photocatalytic performance of monolayer MoS_2 needs further investigation by SVET. A large area of monolayer might be achieved by the atomic layer deposition technique. The correlation between the activity of monolayer MoS_2 and the wavelength of illuminated light can be explored. Additionally, the thickness-dependent activity could be further discovered by using CVD-grown MoS_2 film for ATR-FTIR analysis.

A

Appendix: SEM & EDS

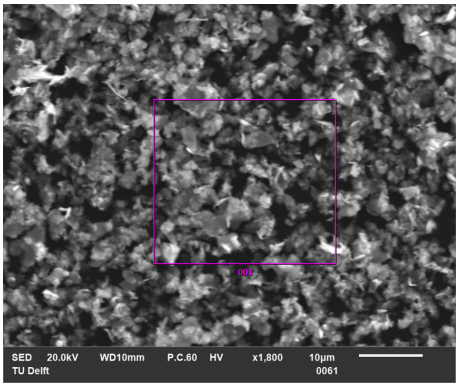

	mass%	Atom%	Line
C	59.00	78.99	K
O	1.40	1.41	K
F	13.58	11.49	K
S	10.48	5.26	K
K	1.03	0.42	K
Mo	14.51	2.43	L
Total	100.00	100.00	

Figure A.1: SEM image and EDS result of MoS_2@GCE after 2 CV cycles where the potential swept from +4.70 to -2.20 V vs. RHE.

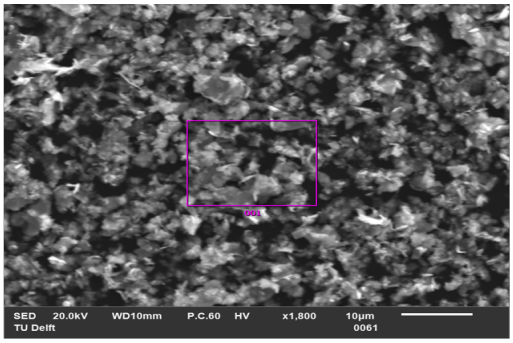

Pure	mass%	Atom%	Line
C	57.46	79.86	K
F	11.75	10.33	K
S	12.04	6.27	K
K	1.14	0.49	K
Mo	17.61	3.06	L
Total	100.00	100.00	

Oxide	mass%	Atom%	Line
C	43.65	80.56	K
F	7.45	8.70	K
SO_3	25.43	7.04	K
K_2O	1.11	0.26	K
MoO_3	22.35	3.44	L
Total	100.00	100.00	

Figure A.2: SEM image and EDS result of MoS_2@GCE after 2 CV cycles where the potential swept from +4.70 to -2.20 V vs. RHE.

(a) **(b)**

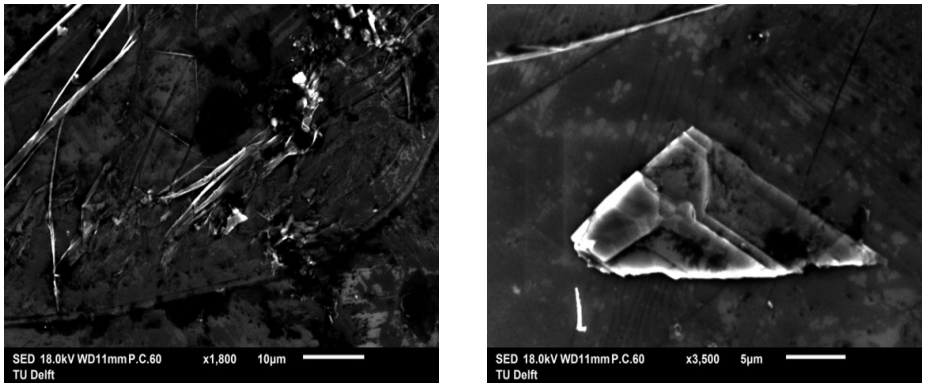

Figure A.3: SEM images of the bulk MoS_2.

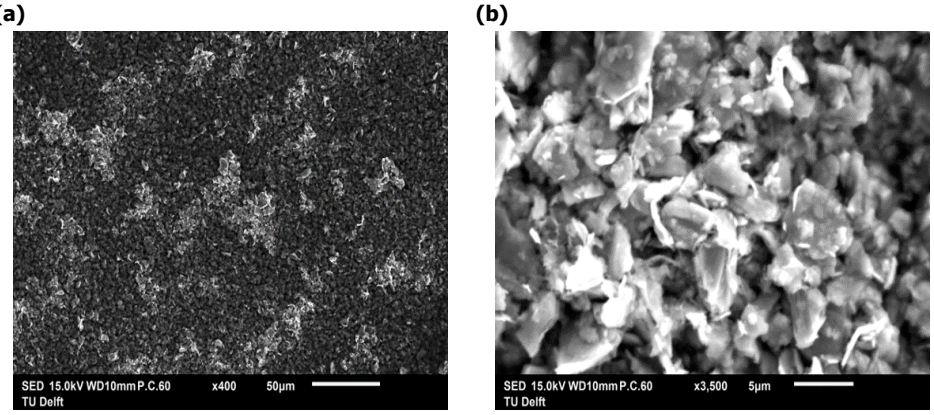

Figure A.4: SEM images of drop-casted MoS_2@GCE.

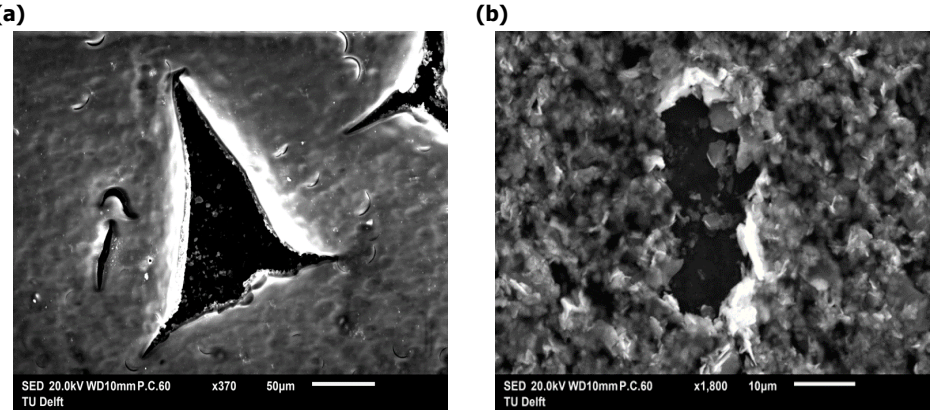

Figure A.5: SEM images of drop-casted MoS_2 @GCE after the GC measurement (a constant potential of -0.806V vs. RHE was applied for 1 hour in CO_2-saturated 0.1M $KHCO_3$ solution).

Bibliography

[1] S. A. Kulp and B. H. Strauss, *New elevation data triple estimates of global vulnerability to sea-level rise and coastal flooding,* Nat Commun **10**, 4844 (2019).

[2] A. Vaughan, *Ipcc report: Sea levels could be a metre higher by 2100,* New Scientist (2019).

[3] Masson-Delmotte, Valérie, *et al.*, *Global warming of 1.5 °c,* An IPCC Special Report on the impacts of global warming of 1.5 °C (2018).

[4] National Oceanic and Atmospheric Administration, *Ocean acidification,* (2020).

[5] A. Buis, *The atmosphere: Getting a handle on carbon dioxide,* NASA's Jet Propulsion Laboratory (2019).

[6] X. Zhang, S. Guo, K. A. Gandionco, A. M. Bond, and J. Zhang, *Electrocatalytic carbon dioxide reduction: from fundamental principles to catalyst design,* Materials Today Advances **7**, 100074 (2020).

[7] United States Environmental Protection Agency, *Global greenhouse gas emissions data,* (Accessed 16 Sep. 2020).

[8] S. Nyquist, *Energy 2050: Insights from the ground up,* (2016).

[9] X. Hu and K. Daasbjerg, *Molecular catalyst converts carbon dioxide to methanol,* (2019).

[10] E. V. Kondratenko, G. Mul, J. Baltrusaitis, G. O. Larrazábal, and J. Pérez-Ramírez, *status and perspectives of co_2 conversion into fuels and chemicals by catalytic, photocatalytic and electrocatalytic processes,* Energy & environmental science **6**, 3112 (2013).

[11] Y. Y. Birdja, E. Pérez-Gallent, M. C. Figueiredo, A. J. Göttle1, F. Calle-Vallejo, and M. T. M. Koper, *Advances and challenges in understanding the electrocatalytic conversion of carbon dioxide to fuels,* Nature Energy **4**, 732 (2019).

[12] Y. Zheng *et al.*, *Energy related co_2 conversion and utilization: Advanced materials/ nanomaterials, reaction mechanisms and technologies,* Nano Energy **40**, 512 (2017).

[13] Z. Sun, T. Ma, H. Tao, Q. Fan, and B. Han, *Fundamentals and challenges of electrochemical co2 reduction using two-dimensional materials,* Chem **3**, 560 (2017).

[14] P. Abbasi *et al.*, *Tailoring the edge structure of molybdenum disulfide toward electrocatalytic reduction of carbon dioxide,* ACS nano **11**, 453 (2017).

[15] H. Tao, X. Sun, S. Back, Z. Han, Q. Zhu, A. W. Robertson, T. Ma, Q. Fan, B. Han, Y. Jung, *et al.*, *Doping palladium with tellurium for the highly selective electrocatalytic reduction of aqueous co 2 to co,* Chemical science **9**, 483 (2018).

[16] S. Nitopi *et al.*, *Progress and perspectives of electrochemical co2 reduction on copper in aqueous electrolyte,* Chemical reviews **119**, 7610 (2019).

[17] S. Liang, N. Altaf, L. Huang, Y. Gao, and Q. Wang, *Electrolytic cell design for electrochemical co2 reduction,* Journal of CO2 Utilization **35**, 90 (2020).

[18] P. Lobaccaro, M. R. Singh, E. L. Clark, Y. Kwon, A. T. Bell, and J. W. Ager, *Effects of temperature and gas-liquid mass transfer on the operation of small electrochemical cells for the quantitative evaluation of co 2 reduction electrocatalysts,* Physical Chemistry Chemical Physics **18**, 26777 (2016).

[19] A. J. Bard and L. R. F. and, *Fundamentals and applications,* Electrochemical Methods **2**, 580 (2001).

[20] M. Dunwell, Y. Yan, and B. Xu, *Understanding the influence of the electrochemical double-layer on heterogeneous electrochemical reactions,* Current opinion in chemical engineering **20**, 151 (2018).

[21] A. Murata and Y. Hori, *Product selectivity affected by cationic species in electrochemical reduction of co2 and co at a cu electrode,* Bulletin of the Chemical Society of Japan **64**, 123 (1991).

[22] M. R. Thorson, K. I. Siil, and P. J. A. Kenis, *Effect of cations on the electrochemical conversion of co2 to co,* Journal of the Electrochemical Society **160**, F69 (2012).

[23] Y. Hori, A. Murata, and R. Takahashi, *Formation of hydrocarbons in the electrochemical reduction of carbon dioxide at a copper electrode in aqueous solution,* Journal of the Chemical Society, Faraday Transactions 1: Physical Chemistry in Condensed Phases **85**, 2309 (1989).

[24] M. König, J. Vaes, E. Klemm, and D. Pant, *Solvents and supporting electrolytes in the electrocatalytic reduction of co2,* Iscience **19**, 135 (2019).

[25] D. Yang, Q. Zhu, and B. Han, *Electroreduction of co2 in ionic liquid-based electrolytes,* The Innovation **1**, 100016 (2020).

[26] J. D. Faggion, W. D. Goncalves, and J. Dupont, *Co_2 electroreduction in ionic liquids,* Frontiers in Chemistry **7**, 102 (2019).

[27] M. Asadi *et al.*, *Robust carbon dioxide reduction on molybdenum disulphide edges,* Nature communications **5**, 1 (2014).

[28] M. Moura de Salles Pupo and R. Kortlever, *Electrolyte effects on the electrochemical reduction of co2,* ChemPhysChem **20**, 2926 (2019).

[29] J. Liang, H. Tan, M. Liu, B. Liu, N. Wang, Q. Zhang, Y. Zhao, A. H. Smets, M. Zeman, and X. Zhang, *A thin-film silicon based photocathode with a hydrogen doped tio 2 protection layer for solar hydrogen evolution,* Journal of Materials Chemistry A **4**, 16841 (2016).

[30] L. Wang, C.-Y. Lee, and P. Schmuki, *Solar water splitting: preserving the beneficial small feature size in porous α-fe 2 o 3 photoelectrodes during annealing,* Journal of Materials Chemistry A **1**, 212 (2013).

[31] M. J. Kenney, M. Gong, Y. Li, J. Z. Wu, J. Feng, M. Lanza, and H. Dai, *High-performance silicon photoanodes passivated with ultrathin nickel films for water oxidation,* Science **342**, 836 (2013).

[32] D. L. T. Nguyen, Y. Kim, Y. J. Hwang, and D. H. Won, *Progress in development of electrocatalyst for co2 conversion to selective co production,* Carbon Energy **2**, 72 (2020).

[33] Y. Xie *et al.*, *Reaction mechanisms for reduction of co2 to co on monolayer mos2,* Applied Surface Science **499**, 143964 (2020).

[34] M. Asadi *et al.*, *Nanostructured transition metal dichalcogenide electrocatalysts for co2 reduction in ionic liquid,* Science **353**, 467 (2016).

[35] X. Hong, K. Chan†, C. Tsai, and J. K. Nørskov, *How doped mos2 breaks transition-metal scaling relations for co2 electrochemical reduction,* Acs Catalysis **6**, 4428 (2016).

[36] X. Li and H. Zhu, *Two-dimensional mos2: Properties, preparation, and applications,* Journal of Materiomics **1**, 33 (2015).

[37] D. Voiry, A. Mohite, and M. Chhowalla, *Phase engineering of transition metal dichalcogenides,* Chemical Society Reviews **44**, 2702 (2015).

[38] Z. Li, X. Meng, and Z. Zhang, *Recent development on mos2-based photocatalysis: A review,* Journal of Photochemistry and Photobiology C: Photochemistry Reviews **35**, 39 (2018).

[39] R. J. Toh, Z. Sofer, J. Luxa, D. Sedmidubský, and M. Pumera, *3r phase of mos2 and ws2 outperforms the corresponding 2h phase for hydrogen evolution,* Chemical Communications **53**, 3054 (2017).

[40] X. Gan *et al.*, *2h/1t phase transition of multilayer mos2 by electrochemical incorporation of s vacancies,* ACS Applied Energy Materials **1**, 4754 (2018).

[41] Y. Yuan, H. Lu, Z. Yu, and Z. Zou, *Noble□metal□free molybdenum disulfide cocatalyst for photocatalytic hydrogen production,* ChemSusChem **8**, 4113 (2015).

[42] Ossila, *Molybdenum disulfide (mos2): Theory & applications,* (Accessed 4 Oct. 2020).

[43] Y. Li, Y. L. Li, C. M. Araujo, W. Luo, and R. Ahuja, *Single-layer mos_2 as an efficient photocatalyst. catalysis science & technology,* Catalysis Science & Technology **3**, 2214 (2013).

[44] L. Yu, Y. Xie, J. Zhou, Y. Li, Y. Yu, and Z. Ren, *Robust and selective electrochemical reduction of co_2: the case of integrated 3d tio_2@ mos_2 architectures and ti–s bonding effects,* Journal of Materials Chemistry A **6**, 4706 (2018).

[45] J. Greeley, T. F. Jaramillo, J. Bonde, I. Chorkendorff, and J. K. Norskov, *Computational high-throughput screening of electrocatalytic materials for hydrogen evolution,* Nature materials **5**, 909 (2006).

[46] nanoComposix, *Depositing monolayers & thin films of nanoparticles,* (2020).

[47] P. Ghosh and S. Powar, *Manufacturing techniques of perovskite solar cells. in applications of solar energy,* Springer **341–364** (2018).

[48] A. C. Bastos, M. C. Quevedo, O. V. Karavai, and M. G. S. Ferreira, *On the application of the scanning vibrating electrode technique (svet) to corrosion research.* Journal of The Electrochemical Society **164**, C973 (2017).

[49] Y. Gonzalez-Garcia, S. Garcia, and J. Mol, *Electrochemical techniques for the study of self healing coatings,* in *Active Protective Coatings* (Springer, 2016) pp. 203–240.

[50] S. Aryal, *Gas chromatography- definition, principle, working, uses,* (2018).

[51] C. Engineering and G. T. Delft), *Gas chromatography (gc),* (Accessed 18 Oct. 2020).

[52] D. Harvey, *12.4: Gas chromatography,* (2020).

[53] Linde, *Thermal conductivity detector (tcd),* (Accessed 16 Nov. 2020).

[54] GAS, *Compactgc4.0),* (Accessed 16 Nov. 2020).

[55] Shimadzu, *6. detector,* (Accessed 16 Nov. 2020).

[56] M. TOLEDO, *Attenuated total reflectance (atr) sampling technology for ftir applications,* (Accessed 31 Oct. 2020).

[57] A. Paar, *Attenuated total reflectance (atr),* (Accessed 31 Oct. 2020).

[58] L. Jin and A. Seifitokaldani, *In situ spectroscopic methods for electrocatalytic co2 reduction,* Catalysts **10**, 481 (2020).

[59] A. M. Pinto, V. B. Oliveira, and D. S. Falcão, *Direct alcohol fuel cells for portable applications: fundamentals, engineering and advances,* Academic Press , 113 (2018).

[60] T. U. of UTAH, *Electron microscopy tutorial,* (Accessed 1 Nov. 2020).

[61] T. U. of Waikato, *Magnification and resolution,* (Accessed 1 Nov. 2020).

[62] A. Nanakoudis, *Edx analysis with sem: How does it work?* (2019).

[63] R. P. Gangloff and B. P. Somerday, *Gaseous hydrogen embrittlement of materials in energy technologies: the problem, its characterisation and effects on particular alloy classes* (Elsevier, 2012).

[64] L. Fan, C. Xia, F. Yang, J. Wang, H. Wang, and Y. Lu, *Strategies in catalysts and electrolyzer design for electrochemical co2 reduction toward c2+ products,* Science Advances **6**, eaay3111 (2020).

[65] H. Zhong, K. Fujii, and Y. Nakano, *Effect of khco$_3$ concentration on electrochemical reduction of co$_2$ on copper electrode,* Journal of The Electrochemical Society **164**, 9 (2017).

[66] A. Hailu and S. K. Shaw, *Efficient electrocatalytic reduction of carbon dioxide in 1-ethyl-3-methylimidazolium trifluoromethanesulfonate and water mixtures,* Energy & Fuels **32**, 12695 (2018).

[67] C. B. Hiragond, H. Kim, J. Lee, S. Sorcar, C. Erkey, and S.-I. In, *Electrochemical co2 reduction to co catalyzed by 2d nanostructures,* Catalysts **10**, 98 (2020).

[68] A. Angulo, P. van der Linde, H. Gardeniers, M. Modestino, and D. F. Rivas, *Influence of bubbles on the energy conversion efficiency of electrochemical reactors,* Joule **4**, 555 (2020).

[69] M. Khan, *Size-dependent quantization effect in optical properties of mos2 nanostructures,* ChemistrySelect **4**, 2116 (2019).

[70] K. Chang, M. Li, T. Wang, S. Ouyang, P. Li, L. Liu, and J. Ye, *Drastic layer-number-dependent activity enhancement in photocatalytic h2 evolution over nmos2/cds (n≥ 1) under visible light,* Advanced Energy Materials **5**, 1402279 (2015).

[71] K. U. Calvinho, A. B. Laursen, K. M. Yap, T. A. Goetjen, S. Hwang, N. Murali, B. Mejia-Sosa, A. Lubarski, K. M. Teeluck, E. S. Hall, *et al.*, *Selective co$_2$ reduction to c$_3$ and c$_4$ oxyhydrocarbons on nickel phosphides at overpotentials as low as 10 mv,* Energy & Environmental Science **11**, 2550 (2018).

[72] G. Shi, L. Yu, X. Ba, X. Zhang, J. Zhou, and Y. Yu, *Copper nanoparticle interspersed mos_2 nanoflowers with enhanced efficiency for co 2 electrochemical reduction to fuel,* Dalton Transactions **46**, 10569 (2017).

[73] F. Bollino, E. Armenia, and E. Tranquillo, *Zirconia/hydroxyapatite composites synthesized via sol-gel: Influence of hydroxyapatite content and heating on their biological properties,* Materials **10**, 757 (2017).

[74] S. Zhu, B. Jiang, W.-B. Cai, and M. Shao, *Direct observation on reaction intermediates and the role of bicarbonate anions in co2 electrochemical reduction reaction on cu surfaces,* Journal of the American Chemical Society **139**, 15664 (2017).

[75] S. Zhu, T. Li, W.-B. Cai, and M. Shao, *Co_2 electrochemical reduction as probed through infrared spectroscopy,* ACS Energy Letters **4**, 682 (2019).

[76] A. Wuttig, C. Liu, Q. Peng, M. Yaguchi, C. H. Hendon, K. Motobayashi, S. Ye, M. Osawa, and Y. Surendranath, *Tracking a common surface-bound intermediate during co2-to-fuels catalysis,* ACS central science **2**, 522 (2016).

[77] D. Kim, S. Lee, J. D. Ocon, B. Jeong, J. K. Lee, and J. Lee, *Insights into an autonomously formed oxygen-evacuated cu_2o electrode for the selective production of c_2h_2 from co_2,* Physical Chemistry Chemical Physics **17**, 824 (2015).

[78] D. McAteer, Z. Gholamvand, N. McEvoy, A. Harvey, E. O'Malley, G. S. Duesberg, and J. N. Coleman, *Thickness dependence and percolation scaling of hydrogen production rate in mos2 nanosheet and nanosheet–carbon nanotube composite catalytic electrodes,* ACS nano **10**, 672 (2016).

[79] S. Hao, X. Shen, M. Tian, R. Yu, Z. Wang, and L. Chen, *Reversible conversion of mos_2 upon sodium extraction,* Nano Energy **41**, 217 (2017).

[80] E. Benavente, M. Santa Ana, F. Mendizábal, and G. González, *Intercalation chemistry of molybdenum disulfide,* Coordination chemistry reviews **224**, 87 (2002).

[81] C. G. Hawkins and L. Whittaker-Brooks, *Controlling sulfur vacancies in tis2–x cathode insertion hosts via the conversion of tis3 nanobelts for energy-storage applications,* ACS Applied Nano Materials **1**, 851 (2018).

[82] O. Brontvein, R. Tenne, and A. Enyashin, *The role of lead (pb) in the high temperature formation of mos2 nanotubes,* Inorganics **2**, 363 (2014).

[83] D. E. Newbury, *Mistakes encountered during automatic peak identification of minor and trace constituents in electron-excited energy dispersive x-ray microanalysis,* Scanning: The Journal of Scanning Microscopies **31**, 91 (2009).

[84] Thermofisher, *Carbon,* (Accessed 11 Nov. 2020).

[85] Y. Cai, X. Yang, T. Liang, L. Dai, L. Ma, G. Huang, W. Chen, H. Chen, H. Su, and M. Xu, *Easy incorporation of single-walled carbon nanotubes into two-dimensional mos2 for high-performance hydrogen evolution,* Nanotechnology **25**, 465401 (2014).

[86] Thermofisher, *Oxygen,* (Accessed 18 Nov. 2020).

[87] NIST, *Nist x-ray photoelectron spectroscopy database,* (Accessed 18 Nov. 2020).

[88] J. Iranmahboob, S. D. Gardner, H. Toghiani, and D. O. Hill, *Xps study of molybdenum sulfide catalyst exposed to co and h_2,* Journal of colloid and interface science **270**, 123 (2004).

[89] S. Hong, C. K. Rhee, and Y. Sohn, *Photoelectrochemical hydrogen evolution and co2 reduction over mos2/si and mose2/si nanostructures by combined photoelectrochemical deposition and rapid-thermal annealing process,* Catalysts **9**, 494 (2019).